Systematic X-ray Spectral Study of Particle Acceleration in Supernova Remnants

(X線スペクトルによる超新星残骸における粒子加速の系統的研究)

2016年9月

埼玉大学大学院理工学研究科(博士後期課程)
理工学専攻(主指導教員　田代　信)

武田　佐和子

SYSTEMATIC X-RAY SPECTRAL STUDY OF PARTICLE ACCELERATION IN SUPERNOVA REMNANTS

Sawako Takeda

Department of Physics, Graduate School of Science, Saitama University
Shimo-Okubo, Sakura-ku, Saitama, 338-8570, Japan
`takeda@heal.phy.saitama-u.ac.jp`

Thesis submitted to the Department of Physics,
Graduate School of Science, Saitama University
on June, 2016
in partial fulfillment of the requirements
for the degree of Doctor of Philosophy in physics

September 4, 2016

Contents

1 Introduction **11**

2 Review **13**

2.1 Cosmic-ray Acceleration . . . 14
  2.1.1 Cosmic Ray . . . 14
  2.1.2 Diffusive Shock Acceleration . . . 14
2.2 X-ray Emission from Cosmic-rays . . . 18
  2.2.1 Synchrotron Emission . . . 18
  2.2.2 Inverse Compton Scattering . . . 19
  2.2.3 π_0 Decay Emission . . . 20
2.3 Supernova Remnant . . . 20
  2.3.1 SNRs as Sources of Galactic Cosmic Rays . . . 20
  2.3.2 Evolution of SNRs . . . 21
    Free Expansion Phase . . . 21
    Sedov Phase (Adiabatic Phase) . . . 22
    Radiative Cooling Phase (Snowplow Phase) . . . 22
    Disappearance Phase . . . 23

2.3.3 Characteristic Energy and Spectral Shape by Accerelated Particles in SNRs . . . 23

Characteristic Energy . . . 23

Spectral Shape . . . 24

2.3.4 Individual Objects . . . 26

2.4 Scope of This Work . . . 27

3 Instruments onboard Suzaku **29**

3.1 Overview of the Suzaku X-ray Observatory . . . 29

3.2 X-ray Imaging Spectrometer — XIS . . . 31

3.3 Hard X-ray Detector — HXD . . . 34

4 Observation and Data reduction **39**

4.1 Target Selection . . . 39

4.2 Observations . . . 40

4.2.1 Vela Jr. . . . 40

4.3 Data Reduction . . . 43

4.3.1 XIS . . . 43

4.3.2 HXD-PIN . . . 43

4.4 Estimation of Backgrounds . . . 43

5 Analysis and Results **45**

5.1 XIS Analysis . . . 46

5.1.1 Imaging Analysis . . . 46

5.1.2 Spectral Analysis . . . 46

5.2 HXD Analysis . . . 47

5.2.1 Estimation of Reproducibility of NXB model 47
5.2.2 Calculation of Angular Response 50
5.2.3 Spectral Analysis 50
5.3 Joint Spectrum 55

6 Discussion 59

6.1 Vela Jr. 59
6.2 Relation of photon indices described by Yamazaki et al. 60
6.3 Imaging analysis of the outlier SNRs 62

7 Conclusion 67

List of Figures

2.1 The diagram of an encounter at shock front. 16

3.1 The structure of the Suzaku from Mitsuda et al. (2007). 30

3.2 The photo of the XIS from Koyama et al. (2007). 32

3.3 Diagram of CCDs of FI (left) and BI (right).
http://cosmic.riken.jp/suzaku/help/guide/fstep_web/node4.html#SECTION0043000000000000000
. . . . 33

3.4 The structure of the HXD from Takahashi et al. (2007). 35

3.5 The effective area of the HXD PIN and GSO from Takahashi et al. (2007). . 36

3.6 The angular response of the HXD from Takahashi et al. (2007). 37

5.1 The mosaiced XIS image of Vela Jr. in 2–5 keV band. The exposure is corrected, but the CXB is not subtracted. The regions of the calibration sources are removed. The green and magenta boxes show the FOVs of the XIS of all the observations and of the PIN during NW observation, respectively. The coordinates are in the J2000 equatorial system. 46

5.2 The upper panel shows the XIS spectra fitted with a single power-law model in the 2.0–8.0 keV band. The lower panel shows the χ-residuals between the data and best-fit model. The black, red, and green lines denote the XIS 0, 1, and 3 data, respectively. 48

5.3 Forty-two white boxes used to estimate the arf, in which the significant X-ray emission was detected with the XIS (see text). A white circle is the region for estimating the background. The image is the same as Figure 5.1. 52

5.4 The black points in the upper panel show the HXD-PIN spectrum fitted with single power-law model in 12.0–22.0 keV band. The error bars include also the systematic error of the NXB model. The red dotted line shows the contribution from the modeled GRXE. The lower panel shows the χ residuals between the data and best-fit model. 54

5.5 Upper left: The upper panel shows the wide band spectrum fitted with (i) single power-law model in 12.0–22.0 keV band. The systematic error of NXB model is included. The cross normalization is fixed at 1.13, which is the value for a point source. The lower panel shows the residuals between the data and model. Upper right: Same as the upper left except for using (ii) cutoff power-law model. Lower left: Same as the upper left except for using (iii) broken power-law. Lower right: Same as the upper left except for using (iv) 10 keV broken power-law. 56

6.1 The relation between the two X-ray photon indices for soft and hard bands for a breaking power-law model. The straight lines show the theoretical lines derived by Yamazaki et al. (2014). The open squares, triangles and circles are for $BE^2_{\rm max,e} = 10^4$, 10^5, and $10^6 \mu{\rm G}({\rm TeV})^2$, respectively (See Yamazaki et al. (2014)). The black squares and triangles show the result of RX J1713.7−3946 and of Cassiopeia A, respectively. The red and blue circles show this result with model (iv) with cross-normalization fixed to 1.13 or freed, respectively. These error bars show 99% confidence level. 63

6.2 The relation between the diameter and filament width. The red shows outlier and the black shows other SNRs. The filled marker shows w_d and another shows w_u. 65

List of Tables

3.1 Specifications / Characteristics of XIS. 33

3.2 Specifications / Characteristics of HXD. 36

4.1 Property of target SNRs. 40

4.2 The information of observation. Exposure is that of after processing. Except for NW, the HXD exposure is not record since they are not used in this thesis. 40

5.1 The best-fit parameters for a power-law model for the XIS spectra and the PIN spectrum. 49

5.2 The weights for making arfs of the PIN. The pointing IDs are shown in figure 5.3. 53

5.3 The best-fit parameters for the XIS and PIN spectra. 57

Chapter 1

Introduction

The supernova remnant (SNR) is formed by shock waves propagating in the interstellar medium (ISM). In addition to the shock heated ISM in the SNR, evidence is often reported of particle acceleration in the shock surface (e.g. Koyama et al. (1995)). However the detailed mechanism or physical parameters are still not clarified, although the diffusive shock acceleration (DSA; Bell (1978)) is thought to be the most promising model. We observe the accelerated electrons through synchrotron radiation. The observed photon energy spectrum directly reflects energy distribution of the relativistic electrons. The roll-off frequency of photon spectrum is determined by the product of the magnetic field strength and the squared maximum energy of electrons (Reynolds (1998a)); and the magnetic field strength is derived from the width of synchrotron filament (Bamba et al. (2003)) and the time variation (Uchiyama et al. (2007)). Since the roll-off frequency is often observed in the X-ray band particularly from the young SNR, X-ray observation is a key to solve the particle acceleration mechanism in the SNR shock surface.

Synchrotron spectral features here we focus are energy spectral index p, roll-off frequency ν_c as mentioned above, and cutoff shape parameter a indicating shape of roll-off. The spectral index p is determined by both mechanism and environments of acceleration, such as the compression ratio r (Bell 1978). Although $p = 2, (r = 4)$ in case of strong shock, “softer” spectrum ($p > 2$) is often observed from young SNRs (e.g. Abdo et al. (2010)), indicating synchrotron radiative cooling. The cutoff shape parameter a is a function of both maximum energy of electrons and their energy dependence of diffusion coefficient (β). Although Bohm diffusion requires $\beta = 1$, reported smaller values ($\beta \sim 1/3$ or $1/2$; Blandford & Eichler 1987) imply complexed magnetic field structure. (Yamazaki et al. 2014) proposed a method to constrain these parameters space in accordance to X-ray photon indices below and above 10 keV.

We present observation results from two SNRs, in which active particle acceleration is expected, with the X-ray observatory Suzaku. In order to select active accelerator, we selected sources with following criteria among 378 Galactic SNRs summarized by Ferrand & Safi-Harb (2012); (1) bright in hard X-ray band, (2) exhibiting shell structure, (3) being in free expansion phase. After omitting those sources which have nearby contaminant sources within the Suzaku hard X-ray detector field of view, we finally chosed 4 SNRs including Vela Jr. and Tycho from which we present newly analyzed data.

Chapter 2

Review

Contents

2.1 Cosmic-ray Acceleration 14

2.1.1 Cosmic Ray 14

2.1.2 Diffusive Shock Acceleration 14

2.2 X-ray Emission from Cosmic-rays 18

2.2.1 Synchrotron Emission 18

2.2.2 Inverse Compton Scattering 19

2.2.3 π_0 Decay Emission 20

2.3 Supernova Remnant 20

2.3.1 SNRs as Sources of Galactic Cosmic Rays 20

2.3.2 Evolution of SNRs 21

2.3.3 Characteristic Energy and Spectral Shape by Accerelated Particles in SNRs 23

2.3.4 Individual Objects 26

2.4 Scope of This Work 27

2.1 Cosmic-ray Acceleration

2.1.1 Cosmic Ray

Cosmic-ray, discovered by Victor F. Hess in 1912, consists of protons, α-particles, heavier nuclei, electrons, and other particles. The energy spectrum of primary cosmic rays are known to be expressed with power-law functions (at least up to $\sim 10^{20}$ eV),

$$\frac{dN}{dE} \propto \begin{cases} E^{-2.7} & (E < E_{\rm knee}) \\ E^{-3.1} & (E > E_{\rm knee}) \end{cases} ,$$

where $E_{\rm knee}$ ($\sim 10^{15}$eV) is the energy of spectral breaking and called the “knee” energy.

It is considered that the particles below knee energy are accelerated in the Galaxy, since particles below 10^{18} eV have gyro radii smaller than the thickness of the Galactic disk. Trajectories of these particles are bended and randomized by the Galactic magnetic fields, causing large uncertainty of their direction of sources.

The energy spectrum is a clue to use ti identify the sources of Galactic cosmic rays. The observed simple power-law spectrum with the energy index of 2.7 over many decades of energy implies that the particles are accelerated by a statistical mechanism. The diffusive shock accerelation (or the first order Fermi acceleration) is widely accepted as the probable mechanism for this acceleration.

2.1.2 Diffusive Shock Acceleration

The diffusive shock acceleration has been studied by Axford (1981), Drury (1983), Blandford & Eichler (1987), Longair (1981), and Bell (1978).

First, we review the fundamental formulae of the statistical acceleration mechanism of acceleration. Assume a test particle gains energy of ΔE at each encounter with another particle or local magnetic field, the increment of energy by each encounter is described as,

$$\Delta E = \xi E, \tag{2.2}$$

and by n times encounter it becomes is

$$E_n = E_0(1+\xi)^n. \tag{2.3}$$

If a probability of particle escapes is $P_{\rm esc}$, the probability that a particle does not escape even after n times encounter is $(1-P_{\rm esc})^n$. Since the number of encounters to reach to the energy of E is

$$n = \frac{\ln{(E/E_0)}}{\ln{(1+\xi)}}, \tag{2.4}$$

the number of particles having energy larger than E is

$$N(\geq E) \propto \sum_{m=n}^{\infty}(1-P_{\rm esc})^m = \frac{(1-P_{\rm esc})}{P_{\rm esc}} \propto \frac{1}{P_{\rm esc}}(\frac{E}{E_0})^{\gamma}, \tag{2.5}$$

where

$$\gamma = \frac{\ln{[1/(1-P_{\rm esc})]}}{\ln{(1+\xi)}} \approx \frac{P_{\rm esc}}{\xi} = \frac{1}{\xi}\frac{T_{\rm cycle}}{T_{\rm esc}}, \tag{2.6}$$

$T_{\rm cycle}$ is time of a accerelation cycle, and $T_{\rm esc}$ is time to escape from the acceleration field. After accerelation for time t, the maximum number of acceleration $n_{\rm max} = \frac{t}{T_{\rm cycle}}$, then we estimate the test particle energy of

$$E \leq E_0(1+\xi)^{t/T_{\rm cycle}}. \tag{2.7}$$

Equation 2.7 shows the two basic characteristics of the Fermi accerelation.

- In order to accerelate particles to the higher energy, the longer time is needed.
- lifetime of acceleration T_A determine the maximum energy of particles.

The maximum energy can be determined by $t = T_A$, if $T_{\rm cycle}$ does not depend on energy.

Next, we describe details of acceleration to derived ξ and γ. Here we assume the acceleration by a parallel shock as shown in Figure 2.1. "Parallel shock" means a shock perpendicular to the magnetic field. Velocity of the parallel shock is $-\vec{u_1}$, and the velocity of gas relative to the shock is $\vec{u_2}$. The $|u_2|$ is larger than $|u_1|$. The gas velosity in laboratory

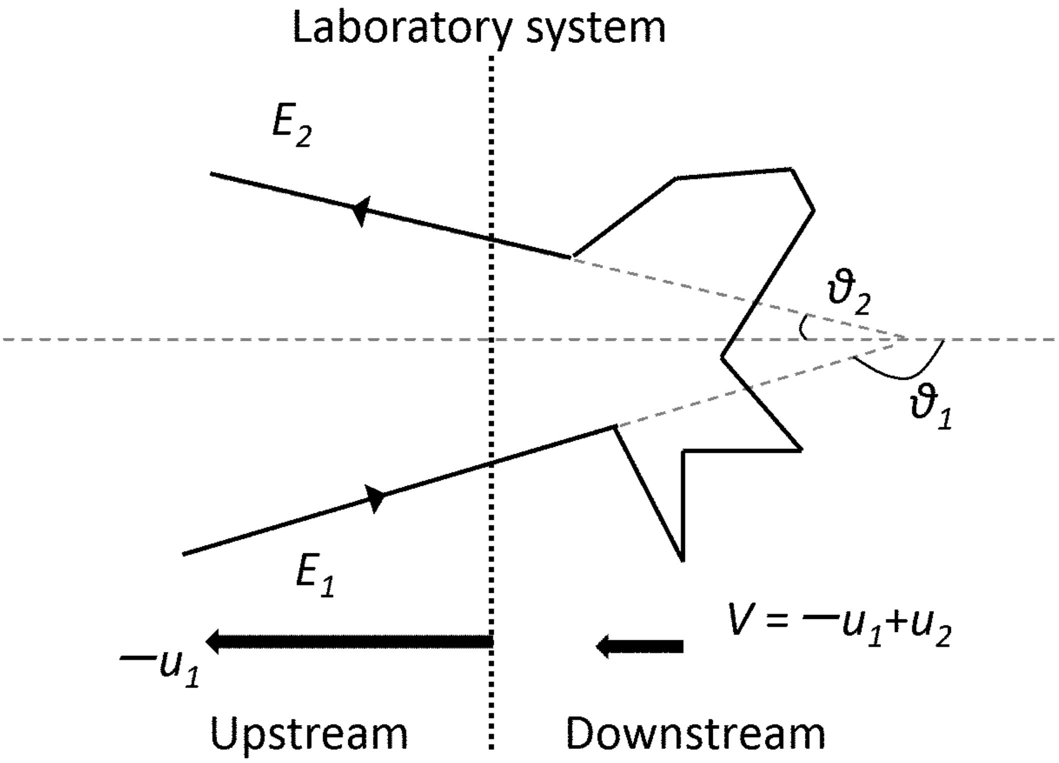
Laboratory system
E_2
ϑ_2
ϑ_1
E_1
$V = -u_1+u_2$
$-u_1$
Upstream
Downstream

Figure 2.1: The diagram of an encounter at shock front.

system is $\vec{V} = -\vec{u_1} + \vec{u_2}$. The relative energy gain of a particle at each encounter is estimated as,

$$\frac{\Delta E}{E_1} = \frac{1 - \beta_{\text{plasma}} \cos\theta_1 + \beta_{\text{plasma}} \cos\theta'_2 - \beta^2_{\text{plasma}} \cos\theta_1 \cos\theta'_2}{1 - \beta^2_{\text{plasma}}} - 1, \tag{2.8}$$

where β_{plasma} is velocity of plasma flow of V/c. For escaping particles,

$$\frac{dn}{d\cos\theta'_2} = 2\cos\theta'_2. \tag{2.9}$$

Since particles can escape only in the left direction of Figure 2.1, we derive the average value within $0 \leq \cos\theta'_2 \leq 1$ as,

$$\langle \cos\theta'_2 \rangle = \frac{2}{3}. \tag{2.10}$$

Therefore we obtain,

$$\frac{\langle \Delta E \rangle_2}{E_1} = \frac{1 - \beta_{\text{plasma}} \cos\theta_1 + \frac{2}{3}\beta_{\text{plasma}} - \frac{2}{3}\beta^2_{\text{plasma}} \cos\theta_1}{1 - \beta^2_{\text{plasma}}} - 1. \tag{2.11}$$

On the other hand, since incident particles have isotropic distribution, then

$$\frac{dn}{d\cos\theta_1} = 2\cos\theta_1. \tag{2.12}$$

Considering $-1 \leq \cos\theta_1 \leq 0$, we derives

$$\langle \cos\theta_1 \rangle = -\frac{2}{3}. \tag{2.13}$$

Therefore,

$$\eta = \frac{1 + \frac{4}{3}\beta_{\text{plasma}} + \frac{4}{9}\beta^2_{\text{plasma}}}{1 - \beta^2_{\text{plasma}}} - 1 \sim \frac{4}{3}\beta_{\text{plasma}} = \frac{4}{3}\frac{u_1 - u_2}{c} \tag{2.14}$$

The acceleration in this case is the "first order Fermi acceleration". This acceleration definitely increases energy of particles.

Considering enough large parallel shock, the possibility of encounter is to be,

$$\int_0^1 d\cos\theta \int_0^{2\pi} \frac{c\rho_{\text{CR}}}{4\pi} \cos\theta = \frac{c\rho_{\text{CR}}}{4} \tag{2.15}$$

where ρ_{CR} is number density of cosmic rays. The flux of particles flowing from the shock front to the downstream is $\rho_{\text{CR}} \times u_2$. Then we estimate,

$$P_{\text{esc}} = \frac{\rho_{\text{CR}} u_2}{c\rho_{\text{CR}}/4} = \frac{4u_2}{c}, \tag{2.16}$$

therefore

$$\gamma = \frac{P_{\rm esc}}{\eta} = \frac{3}{u_1/u_2 - 1}. \tag{2.17}$$

According to continuity of mass at shock front ($\rho_1 u_1 = \rho_2 u_2$) and kinetic theory of gas,

$$\frac{u_1}{u_2} = \frac{\rho_2}{\rho_1} = \frac{(c_p/c_v + 1)M^2}{(c_p/c_v - 1)M^2 + 2} \tag{2.18}$$

where we introduce the sound speed of c_1 and the Mach number Mc_1. In gas of monatomic molecules, $c_p/c_v = 5/3$, then when considering strong shock ($M >> 1$),

$$\gamma \approx 1 + \frac{4}{M^2}. \tag{2.19}$$

Above we assumed "test particle approximation" in which particles does not influence to the acceleration cite. However, actually particles make electromagnetic fluid wave and will be scattered there. Then acceleration will be non-linear, then γ may not be unity. In addition, we ignored injection process of particles. Details discussion of incident particles is described in Blandford & Eichler (1987).

2.2 X-ray Emission from Cosmic-rays

2.2.1 Synchrotron Emission

A particle accelerated up to relativistic velocity emits synchrotron radiation when the traveling direction is bent by a magnetic field $\boldsymbol{B}$. The equation of motion of a particle of mass m and charge q in the magnetic field is

$$\gamma m \boldsymbol{v} = \frac{q}{c} \boldsymbol{v} \times \boldsymbol{B}. \tag{2.20}$$

When we separate $\boldsymbol{v}$ into 2 component along the magnetic field $\boldsymbol{v}_\parallel$ and along the normal of the magnetic field $\boldsymbol{v}_\perp$,

$$\frac{d\boldsymbol{v}_\parallel}{dt} = 0 \tag{2.21}$$

and

$$\frac{d\boldsymbol{v}_\perp}{dt} = \frac{q}{\gamma m c} \boldsymbol{v}_\perp \times \boldsymbol{B}. \tag{2.22}$$

Equation 2.21 shows that $\boldsymbol{v}_{\parallel} = \text{const}$. In contrast Equation 2.22 represents a circular motion. The gyro frequency $\omega_{\rm B} = qB/(\gamma mc)$, and its gyro radius $r_{\rm g} \equiv v/\omega_B = \gamma\beta mc^2/qB$. Acceleration rates are $a_{\parallel} = 0$ and $a_{\perp} = \omega_B v_{\perp}$. The radiation power of the accelerated charged particle is

$$P_{\rm sync} = \frac{2q^2}{3c^3}\gamma^4\left(a_{\perp}^2 + \gamma^2 a_{\parallel}^2\right) = \frac{2q^2}{3c^2}\gamma^4\left(\frac{qB}{\gamma mc}\right)^2\beta_{\perp}^2 c^2. \tag{2.23}$$

When the verosity distribution of particles is isotropic, an average of emission power is derived as

$$\langle\beta_{\perp}^2\rangle = \frac{\beta^2}{4\pi}\int \sin^2\theta d\Omega = \frac{2\beta^2}{3}. \tag{2.24}$$

Therefore Equation 2.23 is rewritten as

$$\langle P_{\rm sync}\rangle = \frac{4q^2}{9c^3}\gamma^4\left(\frac{qB}{\gamma mc}\right)^2\beta^2 c^2 = \frac{4}{3}\sigma_{\rm T} c\beta^2\gamma^2 U_B, \tag{2.25}$$

here $\sigma_{\rm T} = 8\pi r_0^2/3$ is the Thomson's scattering cross-section and $U_B = B^2/8\pi$ is the energy density of magnetic field.

Next, we derive the spectrum of synchrotron emission from electrons with power-law type energy distribution as we see in equation 2.5. Rewrite the equation as

$$N_e(E)dE = CE^{-p}dE, \tag{2.26}$$

and we investigate the contributions of electrons with different energies as

$$\begin{aligned} J(\omega) &= \int P_{\rm sync}(\omega)N_e(E)dE \\ &= \frac{\sqrt{3}e^3 CB\sin\alpha}{2\pi m_e c^2(p+1)}\Gamma\left(\frac{p}{4}+\frac{19}{12}\right)\Gamma\left(\frac{p}{4}-\frac{1}{12}\right)\left(\frac{m_e c\omega}{3eB\sin\alpha}\right)^{-(p-1)/2} \\ &\propto B^{(p+1)/2}\omega^{-(p+1)/2}, \end{aligned} \tag{2.27}$$

where $\Gamma(x)$ is the gamma function of argumrnt x. This shows that the electrons with power-law energy distribution produce synchrotron emission with power-law distribution. The photon index is

$$\Gamma = \frac{p+1}{2}. \tag{2.28}$$

2.2.2 Inverse Compton Scattering

High energy electrons scatter low-energy photons up via the inverse Compton scattering. The cosmic microwave background (CMB) photons are the seed photons in the case of SNRs in general. The TeV gamma-ray emissions observed from some SNRs are often explained as the result of inverse Compton scattering of the CMB photons.

The total power emitted from a single electron via inverse Compton scattering is

$$P_{\rm IC} = \frac{4}{3}\sigma_{\rm T} c \beta^2 \gamma^2 U_{\rm ph}, \tag{2.29}$$

where $U_{\rm ph} = n_{\rm ph}\epsilon_0$ is the energy density of seed photons. Dividing equation 2.25 by equation 2.29 obtain

$$\frac{P_{\rm sync}}{P_{\rm IC}} = \frac{U_{\rm B}}{U_{\rm ph}}. \tag{2.30}$$

If the seed photons are constant, such as in the case of CMB, the magnetic field strength is derived from the ratio of synchrotron emission flux to inverse Compton emission flux.

2.2.3 π_0 Decay Emission

Not only electrons but also high energy protons are though to produce gamma-rays via decay of π_0-mesons. This process provides a unique channel of information about the hadronic component of cosmic-rays.

Protons produce π_0-mesons in inelastic collisions with ambient gas. To produce π_0-mesons, the kinetic energy of protons should exceed $E_{\rm th} = 2m_\pi c^2(1 + m_\pi/4m_p) \approx 280$ MeV. The π_0-mesons decay to two gamma-rays with the mean lifetime of 8.4×10^{17} s, which is significantly shorter than the lifetime of charged π-mesons.

2.3 Supernova Remnant

2.3.1 SNRs as Sources of Galactic Cosmic Rays

Galactic supernova explosions provided that they transfer∼10—20 % of their kinetic energy ($E_{\rm SN} = 10^{51}$erg) into CRs (Hillas2005), assuming two to three supernova explosions per century (Tammann et al.1994).

During a supernova explosion, the ejecta are expelled into the surrounding medium with speeds as large as tens of thousands of kilometers per second. The ejecta carry the kinetic energy of the supernova explosion and cause high Mach number shock fronts in the interstellar medium. Hence, SNRs naturally produces energetic particles by diffusive shock acceleration, with a power-law spectrum with index 2 (e.g., Malkov & Drury (2001a)). The somewhat softer CR spectrum observed in the Earth's, might be explained by propagation effects of CRs through the Galaxy.

The synchrotron emission is observed at radio wavelengths in supernova remnants, revealing the presence of GeV electrons (Shklovskii (1953); Minkowski (1957)). Also, X-ray synchrotron emitting TeV electrons were identified at the shock fronts of the SN 1006 supernova remnant and others (e.g., Koyama et al. (1995)). In the last decade, GeV and TeV gamma-ray emission has been observed from several supernova remnants, indicating the presence of particles with GeV and TeV energies (e.g., Abdo et al. (2010)).

2.3.2 Evolution of SNRs

After a supernova explosion, a stellar ejecta expand into the ambient medium. The ejecta creates shock waves called forward shock and reverse shock. The forward shock sweeps up the ambient medium, and this speed decreases with expanding. The evolution of SNRs are classified in Free Expansion Phase, Sedov Phase (Adiabatic Phase), Radiative Cooling Phase (Snowplow Phase), and Disappearance Phase, according to forward shock speed. The span of shock speed depends on supernova type and its surrounding environment. Now we describe a simple case of type Ia supernova: the number density of interstellar medium $n_0 \sim 1\text{cm}^{-3}$, the temperature of ISM $T_0 \sim 1\text{eV}$, the ejecta mass $M_{\text{ej}} \sim 1M_\odot$, and the energy of supernova explosion $E_{\text{SN}} \sim 10^{51}\text{erg}$. Approximate solutions of other type of supernova are derived in similar way (e.g. Chevalier (1982a)).

Free Expansion Phase

In Free Expansion Phase, the forward shock speed V_s is approximately constant

$$V_0 = \sqrt{\frac{2E}{M_{\text{ej}}}} = 10^9\text{cm s}^{-1}\left(\frac{E_{\text{SN}}}{10^{51}\text{erg}}\right)^{1/2}\left(\frac{M_{\text{ej}}}{1M_\odot}\right)^{-1/2}. \tag{2.31}$$

The forward shock speed decreases slightly since the kinetic energy of the shock dissipate in ambient medium swept up (Chevalier 1982b). When the swept-up mass $4\pi\rho_0 R_s^3/3$ becomes comparable to the ejecta mass, it evolves to Sedov Phase, where ρ_0 is density of the ambient medium and R_s is forward shock radius. At the transition, shock radius is

$$R_{\rm Sedov} = \left(\frac{3M_{\rm ej}}{4\pi\rho_0}\right)^{1/3} = 2.1 \text{ pc} \left(\frac{M_{\rm ej}}{1M_\odot}\right)^{1/3} \left(\frac{n_0}{1 \text{ cm}^{-3}}\right)^{-1/3}, \tag{2.32}$$

and time from supernova is

$$t_{\rm Sedov} = \frac{R_{\rm Sedov}}{V_0} = 210 \text{ yr} \left(\frac{E_{\rm SN}}{10^{51}\text{erg}}\right)^{-1/2} \left(\frac{M_{\rm ej}}{1M_\odot}\right)^{5/6} \left(\frac{n_0}{1 \text{ cm}^{-3}}\right)^{-1/3}. \tag{2.33}$$

These are described in e.g. Truelove & McKee (1999).

Sedov Phase (Adiabatic Phase)

In Sedov Phase, most of energy has transferred from free expanding ejecta to the shock-heated shell, and the SNR expands adiabatically. Radiative cooling is neglected in this phase. When the swept-up mass becomes larger than the ejecta mass, and the total explosion is conserved, then

$$\frac{1}{2}V_s^2 \times \frac{4\pi}{3}\rho_0 R_s^3 = \text{const}. \tag{2.34}$$

The R_s and V_s is expressed as

$$R_s = R_{\rm Sedov}\left(\frac{t}{t_{\rm Sedov}}\right)^{2/5} \tag{2.35}$$

and

$$V_s = \frac{{\rm d}R_s}{{\rm d}t} = \frac{2R_{\rm Sedov}}{5t_{\rm Sedov}}\left(\frac{t}{t_{\rm Sedov}}\right)^{-3/5}. \tag{2.36}$$

When the time from supernova become comparable to the radiative cooling time, it evoluves to Radiative Cooling Phase. The time of transition is expressed as

$$t_{\rm tr} = 2.8 \times 10^4 \text{ yr} \left(\frac{E_{\rm SN}}{10^{51}\text{erg}}\right)^{4/17} \left(\frac{n_0}{1 \text{ cm}^{-3}}\right)^{-9/17} \tag{2.37}$$

in Petruk (2005).

Radiative Cooling Phase (Snowplow Phase)

Since the shock speed is down to below 200 km s^{-1}, the post-shock temperature is less than 5×10^5 K in this phase. Therefore radiation of H, He, C, N, and O line contributes to the radiative cooling. This phase is divided into "the pressure driven snowplow phase" and "the momentum-conserving snowplow phase". The radiuses of these phases are $R_s \propto t^{2/7}$ and $R_s \propto t^{1/4}$ respectively (e.g. Bandiera & Petruk (2004)).

Disappearance Phase

After radiative cooling phase, the shock speed decreases to that of ISM (~ 1 km s^{-1}). In this phase, the shock structure is disappearing. The high temperature component inside of shell is left as a bubble shape structure.

2.3.3 Characteristic Energy and Spectral Shape by Accerelated Particles in SNRs

Characteristic Energy

In this section, we assume the Bohm diffusion, $K(E) \propto E$, for simplicity. More detailed analysis is found in Ohira et al. (2012b). The extension to a more general case ($K(E) \propto E^{\beta}$) is easy and omitted here.

A.1. Maximum energy of accelerated electrons and protons Let v_s and B_d be the shock velocity and the downstream magnetic field, respectively. First, suppose that the maximum energy of electrons is determined from the balance of the synchrotron loss and acceleration. Then, equating the acceleration time

with the synchrotron cooling time,

$$t_{\mathrm{sync}}(E) = 125\ \mathrm{yr}(E/10\ \mathrm{TeV})^{-1}(B_d/100\ \mu\mathrm{G})^{-2}, \tag{2.39}$$

we obtain

$$E_{\mathrm{max}}^{(\mathrm{cool})} = \frac{24}{\xi^{1/2}}\left(\frac{v_s}{10^8\ \mathrm{cm\ s^{-1}}}\right)\left(\frac{B_d}{10\ \mu\mathrm{G}}\right)^{-1/2}\ \mathrm{TeV} \tag{2.40}$$

where ξ is a gyro factor. On the other hand, if the cooling is not significant, that is, $t_{\mathrm{acc}}(E), t_{\mathrm{age}} << t_{\mathrm{sync}}(E)$, then the maximum energy can be determined by the condition $t_{\mathrm{acc}}(E) = t_{\mathrm{age}}$, and we obtain

$$E_{\mathrm{max}}^{(\mathrm{age})} = \frac{4.8\times10^2}{\xi^{1/2}}\left(\frac{v_s}{10^9\ \mathrm{cm\ s^{-1}}}\right)\left(\frac{B_d}{10\ \mu\mathrm{G}}\right)^{-1/2}\left(\frac{t_{\mathrm{age}}}{10^3\ \mathrm{yr}}\right)\ \mathrm{TeV}. \tag{2.41}$$

eliminate V_s^2/ξ and obtain

$$E_{\mathrm{max,p}} \approx 83 \left(\frac{E_{\mathrm{max,e}}}{10\ \mathrm{TeV}}\right)^2 \left(\frac{B_d}{100\ \mu\mathrm{G}}\right)^2 \left(\frac{t_{\mathrm{age}}}{10^3\ \mathrm{yr}}\right)\ \mathrm{TeV} \tag{2.40}$$

On the other hand, the cooling break energy is considered following. Let t be the characteristic time of SNR evolution, which may be the expansion time of t_{age} itself. Then the cooling break, E_{b}, appears in the electron spectrum at the energy where $t_{\mathrm{sync}}(E_b) = t$, that is,

$$E_b = 12.5\ \mathrm{TeV} \left(\frac{t}{10^2\ \mathrm{yr}}\right)^{-1} \left(\frac{B_d}{100\ \mu\mathrm{G}}\right)^{-2}. \tag{2.41}$$

The cooling break appears if $E_b < E_{\mathrm{max,e}} = E_{\mathrm{max}}^{(\mathrm{cool})}$, which can be rewritten as

$$B_d > 139\ \mu\mathrm{G}\xi^{1/3} \left(\frac{V_s}{10^8\ \mathrm{cm\ s^{-1}}}\right)^{-2/3} \left(\frac{t}{10^2\ \mathrm{yr}}\right)^{-2/3}. \tag{2.42}$$

Spectral Shape

First, we show the case of cooling-limited acceleration. Zirakashvili & Aharonian (2007) obtained the asymptotic electron spectrum near the maximum electron energy in the cooling-dominated phase, such as

$$N_e(E) = A_0(E) \exp[S_0(E)], \tag{2.43}$$

$$A_0(E) = E^{-1/2} \exp\left[\int^E \frac{\sqrt{K_2}\frac{\partial}{\partial E}\sqrt{b_2} + \sqrt{K_1}\frac{\partial}{\partial E}\sqrt{b_1}}{\sqrt{b_1 K_1} + \sqrt{b_2 K_2}} dE'\right] \tag{2.44}$$

$$S_0(E) = -\left(\frac{\gamma_s}{V_s}\right)^2 \int^E \left(\frac{\sqrt{b_1 K_1} + \sqrt{b_2 K_2}}{E'}\right)^2, \tag{2.45}$$

where $\gamma_s = 3r/(r-1)$ (r is the shock compression ratio), and V_s is the shock velocity. Functions $K(E)$ and $b(E) = dE/dt$ are the diffusion coefficient and energy loss rate of electrons, respectively. Subscripts 1 and 2 indicate upstream and downstream regions of the shock, respectively. In the case of synchrotron cooling, $b(E)$ is proportional to E^2. We assume that $K(E) = K_0 E^{\Gamma}$ and $b(E) = b_0 E^2$ where K_0 and b_0 are constants, and that ratios b_1/b_2 and K_1/K_2 are also constant. Then we obtain

$$A_0(E) \propto E^{1/2}. \tag{2.46}$$

However, for typical parameters of young SNRs, this positive slope can hardly be seen in the X-ray emission. Furthermore, neglecting non-dimensional terms on the order of unity, we derive

$$S_0(E) \approx -(K_0 b_0/V_s^2)E^{\beta+1}. \tag{2.47}$$

By the way, acceleration time and synchrotron cooling time are calculated as $t_{\mathrm{acc}}(E) \approx K_0 E^{\Gamma}/V_s^2$ and $t_{\mathrm{sync}}(E) \approx (b_0 E)^{-1}$, respectively, where we again neglect terms on the order of unity. Then equating them, we obtain

$$E_{\mathrm{max}}^{(\mathrm{cool})} \approx (V_s^2/K_0 b_0)^{1/(+1)}. \tag{2.48}$$

Therefore, we finally derive

$$S_0(E) \approx -\left(\frac{E}{E_{\mathrm{max}}^{(\mathrm{cool})}}\right)^{\beta+1}. \tag{2.49}$$

Next, we show the case of escape-limited acceleration. We assume the test-particle regime and place a free escape boundary upstream at a distance of l away from the shock front $x = 0$, that is, the particle distribution function is zero at $x = -l(< 0)$. Then the stationary transport equation is solved to find a particle spectrum around the shock front given by (Caprioli et al. 2009; Reville et al. 2009)

$$N_e(E) \approx \exp -\frac{3r}{r-1}\int^{E} \frac{dlogE'}{1-\exp[-V_s l/K(E')]}\ , \tag{2.50}$$

where V_s is the velocity of the shock. In the escape-limited case, the maximum energy is determined by the condition (Ohira et al. 2010)

$$K(E_{\mathrm{max}}^{(\mathrm{esc})})V_s = l. \tag{2.51}$$

Then, one can see

$$K(E)/V_s l = K(E)/K(E_{\mathrm{max}}^{(\mathrm{esc})}) = (E/E_{\mathrm{max}}^{(\mathrm{esc})})^{\beta}. \tag{2.52}$$

Changing variables into

$$y(E') = (E'/E_{\mathrm{max}}^{(\mathrm{esc})})^{\beta}, \tag{2.53}$$

we derive

$$N_e(E) \approx \exp -\frac{3r}{r-1} \times \frac{1}{\beta}\int^{y(E)} \frac{d\log y}{1-e^{-1/y}}\ . \tag{2.54}$$

In the case of $E << E_{\mathrm{max}}^{(\mathrm{esc})}$, the term $e^{-1/y}$ can be neglected, so that we obtain

$$N_e(E) \approx E^{-3r/(r-1)}. \tag{2.55}$$

On the other hand, if $E >> E_{\rm max}^{\rm (esc)}$, we approximate $1 - e^{-1/y} \approx 1/y$, resulting in

$$N_e(E) \approx \exp\left[-(E/E_{\rm max}^{\rm (esc)})\Gamma\right], \tag{2.56}$$

where a term on the order of unity is again neglected.

2.3.4 Individual Objects

I introduce some previous works of SNRs which is analyzed later.

The young SNR Vela Jr. (RX J0852−4622) was discovered by ROSAT in 1998 (Aschenbach 1998). It is one of TeV-emitting SNRs, and has a diameter of 2°. It overlaps with the south-east portion of much larger and known Vela SNR, and is situated near the pulsar and pulsar wind nebulae (PWN) of Vela SNR. Vela Jr. has a synchrotron X-ray shell (Slane et al. (2001), Bamba et al. (2005a)), which is observed also in radio (Combi et al. 1999) and gamma-rays (Aharonian et al. 2005). Fukui (2013) reported a spatial correlation between the radio emission from molecular clouds around Vela Jr. and TeV gamma-rays.

Magnetic field strength at the shock surface of Vela Jr. has been estimated by some authors. Kishishita et al. (2013) derived $B \sim$ 5–20 μG by comparing brightness distribution profile at the shell in 2–10 keV with expected radial profile by Petruk et al. (2011). Lee et al. (2013) performed an MHD simulation of 1D spherically symmetric non-linear diffusive shock acceleration model, and obtained $B \sim 4.8$ μG from observation results, assuming synchron X-rays and cosmic microwave background photon boosted inverse Compton TeV gamma-rays. The observed spectral slope is so steep that we naturally expect the synchrotron rolloff energy below 1 keV and rolloff curvature above. However, the synchrotron emission above 10 keV has not been observed for Vela Jr. by X-ray satellite, and thus have not determine the expected rolloff curvature, yet. In order to determine the photon index and to examine the expected rolloff structure, wideband X-ray observation covering above 10 keV is important.

The Tycho SNR is one of the most brightest SNR and observed by Tycho Brahe in AD 1572. Minkowski (1966) identified a radio source 3C 10 (Hanbury Brown & Hazard 1952) as the Tycho SNR in the radio band. In X-ray band, Friedman et al. (1967) discovered. They found many emission line from highly ionized Mg, Si, S, Ar, Ca, and Fe with ASCA satellite. The cosmic ray acceleration in Tycho has been studied for a long time. Völk et al. (2002) calculated the magnetic field from the wide band spectrum from radio to X-ray to be $\sim 240\mu$G, under the assumption of very efficient acceleration. Hard X-ray emission fro

Tycho was detected up to ~ 30 keV (e.g., Fink et al. (1994) and Tamagawa et al. (2009a)). Non-thermal X-rays should be accompanied by TeV gamma-ray emission. Aharonian et al. (2001) presented the 3 σ upper limit in > 1 TeV. Recently, NuSTAR succeeded in imaging in hard X-ray, up to 40 keV band Lopez et al. (2015).

2.4 Scope of This Work

In this work, I present the photon indices of synchrotron emission of SNRs with particle acceleration actively in X-ray band. Then I study the acceleration mechanism by method of Yamazaki et al. (2014).

Chapter 3

Instruments onboard Suzaku

Contents

3.1 Overview of the Suzaku X-ray Observatory 29

3.2 X-ray Imaging Spectrometer — XIS 31

3.3 Hard X-ray Detector — HXD 34

3.1 Overview of the Suzaku X-ray Observatory

The X-ray astronomical satellite Suzaku was launched in July 2005 Suzaku performed more than 3700 observations with the high sensitivity instruments covering 0.2 to 700 keV band till June 2015, and was terminated in August 2015 due to the life of battery system Mitsuda et al. (2007). Due to the low-earth-orbit of $\sim$ 570 km in altitude, the field of view are often occulted by earth with the orbital period of $\sim$ 96 min. but it realized low particle background thanks to the higher cutoff magnetic rigidity of the earth. However the inclination of 31° inevitably caused observation interruption by passages of the South Atrantic anormaly (SAA), in which the particle backgroound drastically increases.

The side view of Suzaku spacecraft are shown in Figure 3.1. Suzaku has 4 X-ray Imaging Spectrometers (XISs; Koyama et al. (2007)) as soft X-ray detectors and a Hard X-ray Detector (HXD; Takahashi et al. (2007)). Suzaku observes an object with the four XISs and

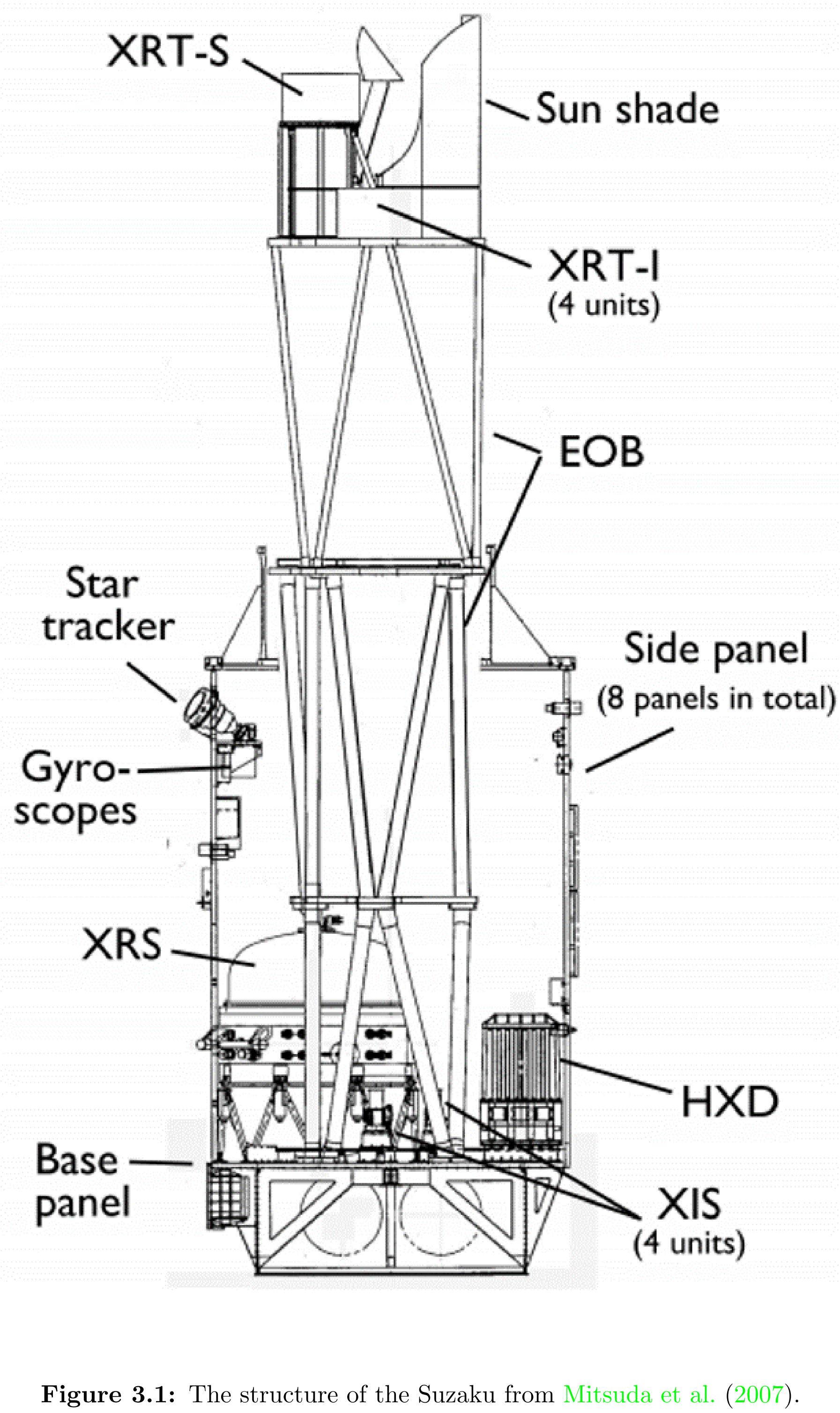
XRT-S
Sun shade
XRT-I
(4 units)
EOB
Star
tracker
Side panel
(8 panels in total)
Gyro-
scopes
XRS
HXD
Base
panel
XIS
(4 units)

Figure 3.1: The structure of the Suzaku from Mitsuda et al. (2007).

the HXD at the same time, therefore we are able to obtain X-ray data with wideband and high sensitivity. In particular, the HXD had the highest sensitivity in 10–300 keV energy range among the hard X-ray instrument in the orbits. Details of each detector are described in section 3.2 and 3.3.

3.2 X-ray Imaging Spectrometer — XIS

The XIS is a X-ray CCD camera. Figure 3.2 shows the XIS sensor. Table 3.1 shows specifications and characteristics of the XISs. Generally an X-ray CCD converts an incident X-ray photon into a charge cloud, with the magnitude of charge which is in proportion to the energy of the absorbed X-ray photon. This charge cloud is transfered by electric field generated by the read out clock, and read out by electrode of the chip.

The XIS has higher sensitivity than that onboard ASCA satellite because of its doubled depth of the depletion layer. The four XISs are named XIS 0, XIS 1, XIS 2, XIS 3. The XIS 0, 2, 3 are front side illuminated (FI) CCDs, whereas the XIS 1 is backside illuminated (BI) CCD. Figure 3.3 shows the diagram of FI and BI CCDs. The FI XISs are sensitive in energy band of > 5 keV, because they have thicker depletion layer than those of BI CCD. In order to calibrate energy in the orbit, a radio isotope calibration sources of ^{55}Fe is installed at two corners of each XIS chip. The irradiated calibration X-rays are Mn Kα (5.9 keV) and Mn Kβ (6.5 keV) and the half-life is 2.7 years. The XIS covers a field of view (FOV) of $17'.8 \times 17'.8$ with the angular resolution of $2'$ in half power diameter in the energy range of 0.2–12 keV. The XIS 2 have not been operated since 2007 due to the damage by micro-meteoroid.

Energy resolusion of the XIS was ~ 130 eV (FWHM) at 5.9 keV at the beginning of life, but charge traps on CCD pixels increases owing to radiation damage in the orbit. Therefore the energy resolution was getting worse to ~ 210 eV (FWHM) at 5.9 keV in August 2006. In order to fill the charge traps, scaced-row charge injection has been performed since September 2006. Then the charge transfer efficiency and the resultant energy resolution is recovered by the operation.

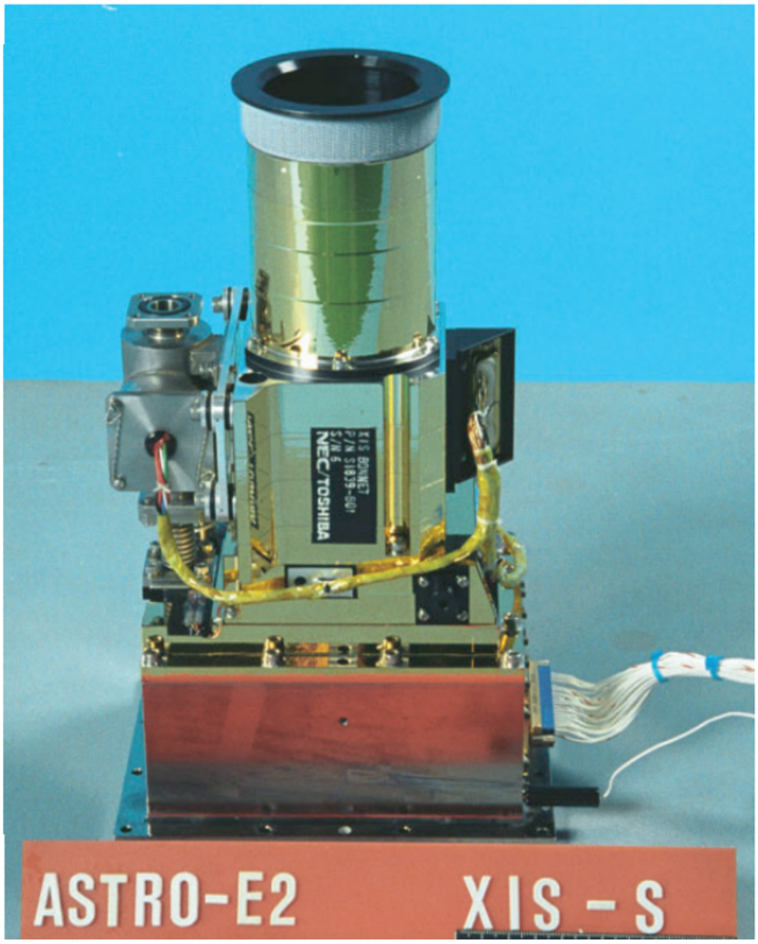
XIS BONNET
NEC/TOSHIBA
ASTRO-E2
XIS - S

Figure 3.2: The photo of the XIS from Koyama et al. (2007).

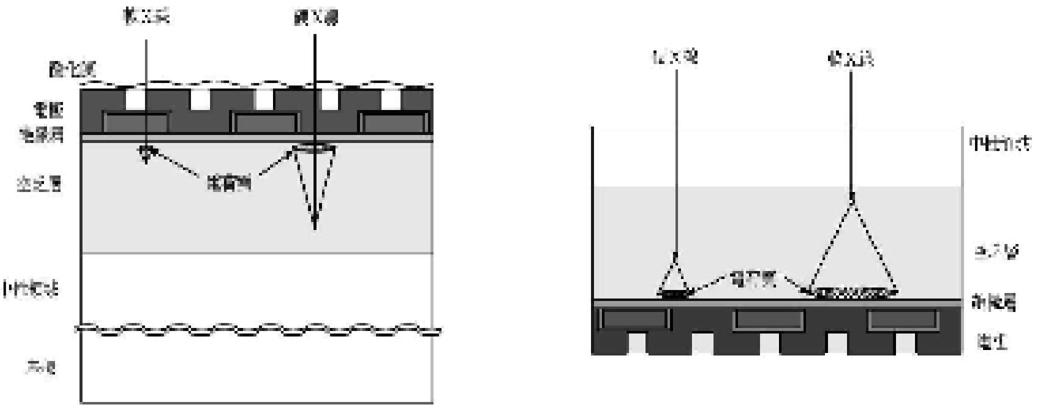

Figure 3.3: Diagram of CCDs of FI (left) and BI (right).
http://cosmic.riken.jp/suzaku/help/guide/fstep_web/node4.html#SECTION00430000000000000000

Table 3.1: Specifications / Characteristics of XIS.

FOV	$17'.8 \times 7'.8$
Energy range	0.2–12 keV
Format	1024×1024 pixels
Pixel Size	$24\ \mu\text{m} \times 24\ \mu\text{m}$
Energy Resolution	~ 130 eV (FWHM) at 5.9 keV
Effective area	330 cm^2 (FI), 370 cm^2 (BI) at 1.5 keV
	160 cm^2 (FI), 110 cm^2 (BI) at 8 keV
Readout Noise	~ 2.5 electrons (RMS)
Time Resolutiom	8 s

3.3 Hard X-ray Detector — HXD

The structure of the HXD is shown in figure 3.4. Table 3.2 shows specifications and characteristics of HXD. The HXD boresight is mis-aligned from the XIS nominal on-axis position by $-3'.5$. The HXD consists of 16 identical well-type phoswich (acronym for phosphor sandwich) counters (Well Unit) and 20 Bismuth germanate crystal (BGO; $Bi_4Ge_3O_{12}$) anti-coincidence counters (Anti Unit). Each Well Unit consists of a p-i-n type silicon detector (PIN) and Gadolinium silicate crystal (GSO; Gd_2SiO_5(Ce)) crystal scintillator, which achieves wide energy range of 10–600 keV. X-rays of ∼10–70 keV are detected by PIN, while X-rays of ∼40–600 keV penetrates PIN and hit GSO below PIN. The backgrounds such as gamma-ray, charged particles, and X-rays from outside of FOV are anti-coincide out by the well type BGO collimator or the Anti Units. Figure 3.5 shows the effective area of the HXD-PIN and GSO.

In addition to the well part active collimator limiting the FOV to $4^\circ.6 \times 4^\circ.6$, installed passive fine collimator made of phosphor bronze limits the low energy range FOV to $0^\circ.56 \times 0^\circ.56$ to reduce source contamination. Figure 3.6 shows angular response of the HXD. Since the well type active shield provides low background environment for the PIN detector, it is one of the ideal detectors to observe low surface brightness objects like SNRs.

The Anti Unit consists of thick (2.6 cm of thickness in average) BGO crystals and phototubes. It works not only as active shield by being set around well unit but also wide band all sky monitor of transient source with the large effective area is ~ 1200 cm^2 and ~ 600 cm^2 at 1 MeV energy photons for each of four sides.

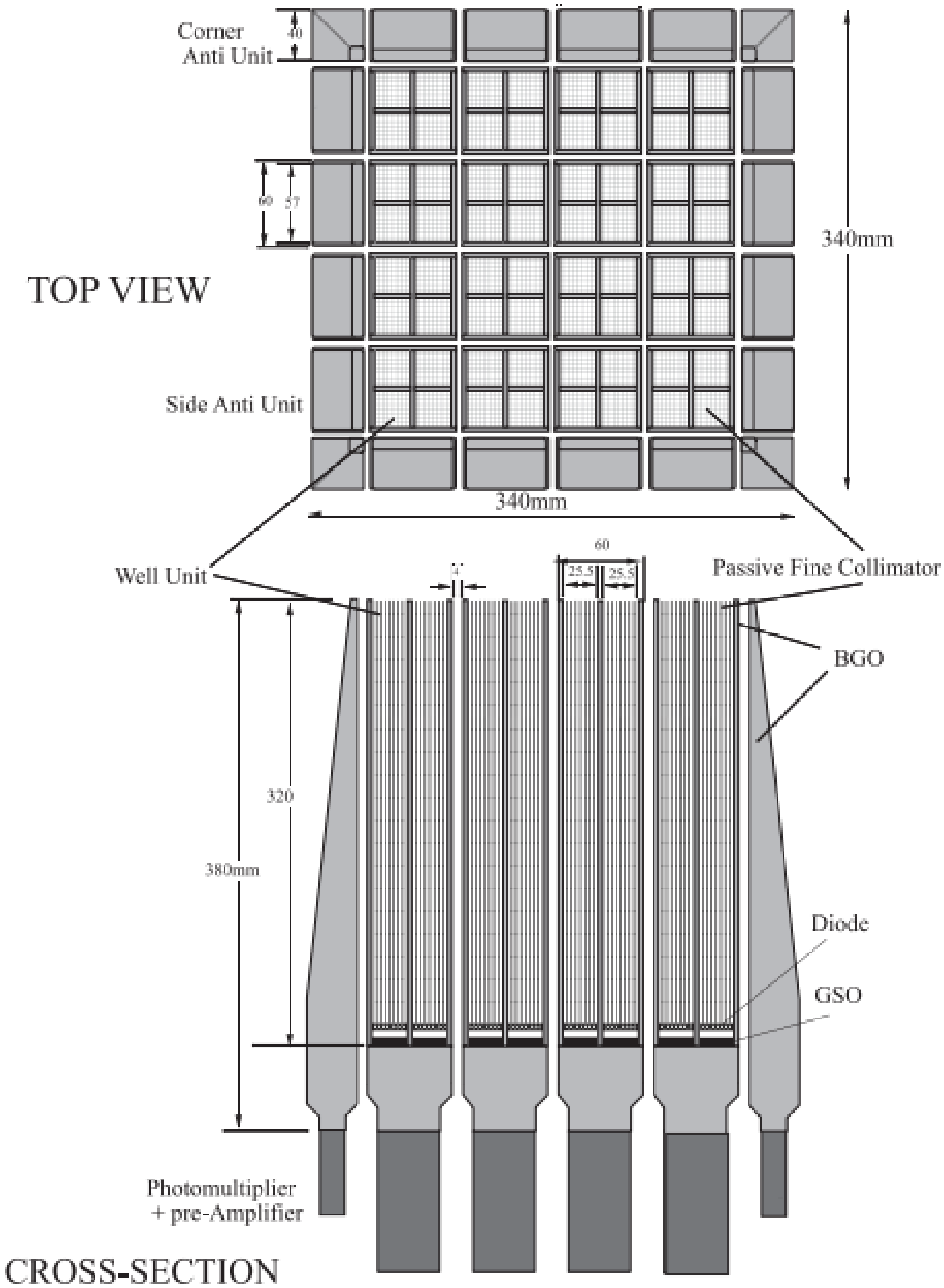
Corner
Anti Unit
40
60
57
340mm
TOP VIEW
Side Anti Unit
340mm
Well Unit
4
60
25.5
25.5
Passive Fine Collimator
BGO
320
380mm
Diode
GSO
Photomultiplier
+ pre-Amplifier
CROSS-SECTION

Figure 3.4: The structure of the HXD from Takahashi et al. (2007).

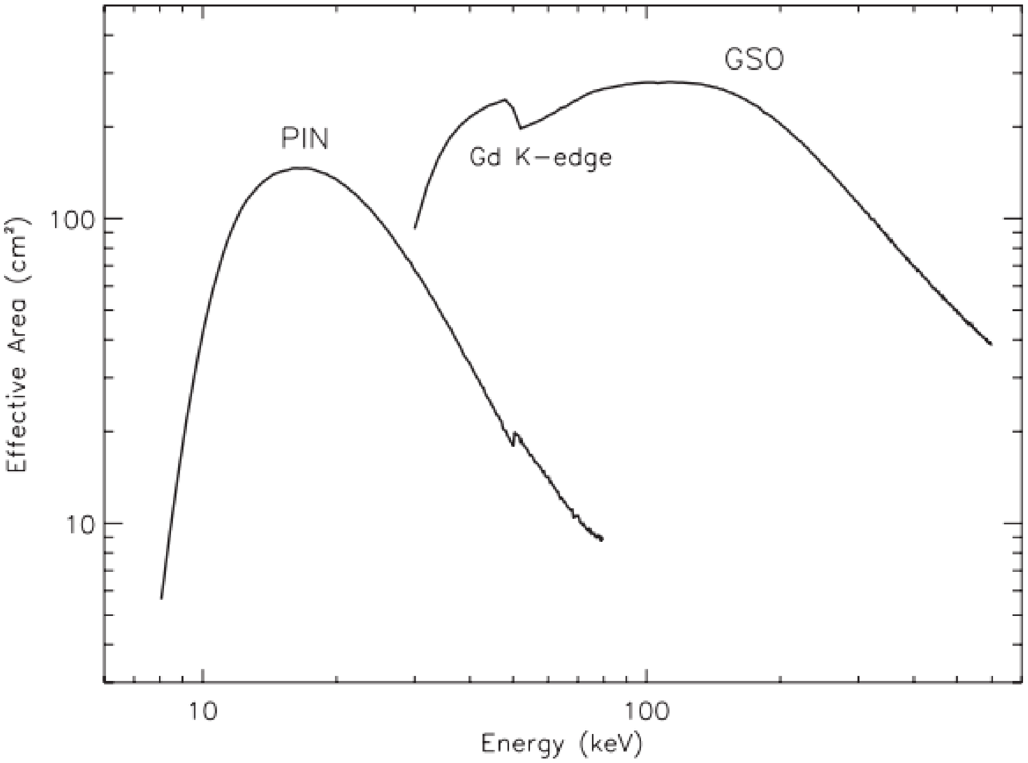

Figure 3.5: The effective area of the HXD PIN and GSO from Takahashi et al. (2007).

Table 3.2: Specifications / Characteristics of HXD.

FOV	$34' \times 34' (\leq 100)$ keV
	$4°.5 \times 4°.5 (\geq 100)$ keV
Energy range	10–600 keV
PIN	10–70 keV
GSO	40–600 keV
Energy Resolution	
PIN	~ 4.0 keV (FWHM)
GSO	$7.0\sqrt{E_{\rm MeV}}$ % (FWHM)
Effective area	$\sim 160 \rm cm^2$ at 20 keV
	$\sim 260 \rm cm^2$ at 100 keV
Time Resolutiom	61 μs or 31 μs

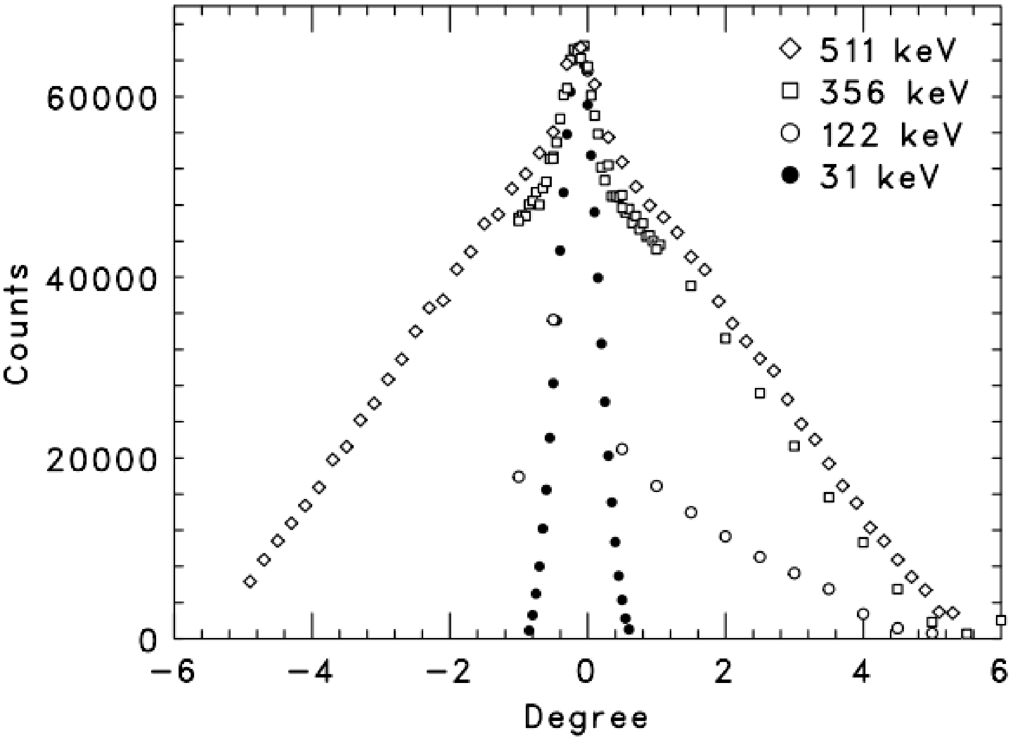

Figure 3.6: The angular response of the HXD from Takahashi et al. (2007).

Chapter 4

Observation and Data reduction

Contents

4.1 Target Selection **39**
4.2 Observations **40**
4.2.1 Vela Jr. 40
4.3 Data Reduction **43**
4.3.1 XIS 43
4.3.2 HXD-PIN 43
4.4 Estimation of Backgrounds **43**

4.1 Target Selection

We selected target SNRs with following criteria (chapter 1):

- the shape shall be a shell-like structure,
- the age shall be less than 5×10^3 yrs,
- the evolution stage shall be free expansion phase, and
- there are no contaminant X-ray sources whose effect are not able to be estimated with good accuracy.

Seven SNRs are selected. Table 4.1 shows the summary of selected SNRs.

All these SNRs except for Vela Jr. has been well studied in previous works. Therefore we analyze the rest SNR, Vela Jr. in this study 4.1.

Table 4.1: Property of target SNRs.

Name	Age [yrs]	Distance [kpc]	Size	Notes
G1.9+0.3	150–200	8.5	$1.5'$	The youngest SNR in the Galaxy.
Kepler	411	2.9–4.9	$3'$	A remnant of the last observed supernova in the Galaxy.
Tycho	443	1.7–5	$8'$	
Vela Jr.	2400–5100	0.5–1	$120'$	Overlapping Vela SNR. The largest source of TeV gamma-ray.
SN 1006	1009	1.6–2.2	$30'$	A remnant of the most brightest supernova in human history.
RX J1713.7−3946	1000–10000	1–6	$65' \times 55'$	Non-thermal dominant SNR.
Cassiopeia A	316–352	3.3 - 3.7	$5'$	One of the brightest radio source.

4.2 Observations

4.2.1 Vela Jr.

We preformed 40 mapping observations of Vela Jr. and its close vicinity in 2005 December, 2007 July, and 2008 July. Table 4.2 shows the observation details. Hereafter, we refer to each observation position in an abbreviated style by clipping each object name. For example, we call Vela Jr P1 as P1, and RXJ_0852−4622_NW as NW.

Table 4.2: The information of observation. Exposure is that of after processing. Except for NW, the HXD exposure is not record since they are not used in this thesis.

Name	ObsID	Date	RA	Dec	Exposure
		YYYY-MM-DD	[deg]	[deg]	XIS / HXD [ks]
VELA JR P1	502023010	2007-07-04	131.98	−45.806	10.7 / –
VELA JR P2	502024010	2007-07-04	132.17	−45.775	8.26 / –
VELA JR P3	502025010	2007-07-04	132.12	−45.604	6.70 / –
VELA JR P4	502026010	2007-07-05	132.52	−45.545	10.3 / –
VELA JR P5	502027010	2007-07-05	132.91	−45.488	10.7 / –
VELA JR P6	502028010	2007-07-05	133.33	−45.485	7.15 / –
VELA JR P7	502029010	2007-07-05	133.78	−45.583	11.8 / –
VELA JR P8	502030010	2007-07-06	133.86	−45.861	13.2 / –
VELA JR P9	502031010	2007-07-06	133.42	−45.763	8.64 / –
VELA JR P10	502032010	2007-07-06	133.00	−45.766	10.2 / –
VELA JR P11	502033010	2007-07-07	132.60	−45.826	11.3 / –
VELA JR P12	502034010	2007-07-08	132.25	−46.051	9.75 / –
VELA JR P13	502035010	2007-07-09	131.85	−46.106	9.41 / –
VELA JR P14	502036010	2007-07-09	131.93	−46.386	10.7 / –
VELA JR P15	502037010	2007-07-10	132.33	−46.329	8.88 / –
VELA JR P16	502038010	2007-07-10	132.68	−46.105	15.1 / –
VELA JR P17	502039010	2007-07-10	133.09	−46.046	7.83 / –
VELA JR P18	502040010	2007-07-10	133.51	−46.042	12.8 / –
VELA JR P19	503031010	2008-07-03	133.98	−46.148	17.7 / –
VELA JR P20	503032010	2008-07-04	133.62	−46.327	13.4 / –
VELA JR P21	503033010	2008-07-04	133.20	−46.330	11.8 / –
VELA JR P22	503034010	2008-07-05	132.44	−46.613	14.7 / –
VELA JR P23	503035010	2008-07-05	132.79	−46.395	10.7 / –
VELA JR P24	503036010	2008-07-05	132.03	−46.673	12.4 / –
VELA JR P25	503037010	2008-07-06	132.52	−46.892	11.4 / –
VELA JR P26	503038010	2008-07-06	132.88	−46.669	10.7 / –
VELA JR P27	503039010	2008-07-06	133.28	−46.606	11.0 / –
VELA JR P28	503040010	2008-07-07	133.71	−46.604	10.9 / –
VELA JR P29	503041010	2008-07-07	134.07	−46.430	8.04 / –
VELA JR P30	503042010	2008-07-07	134.17	−46.704	10.1 / –

Name	ObsID	Date YYYY-MM-DD	RA [deg]	Dec [deg]	Exposure XIS / HXD [ks]
VELA JR P31	503043010	2008-07-08	133.80	−46.885	10.6 / –
VELA JR P32	503044010	2008-07-08	133.37	−46.887	7.64 / –
VELA JR P33	503045010	2008-07-08	133.47	−47.162	11.0 / –
VELA JR P34	503046010	2008-07-09	132.11	−46.950	10.6 / –
VELA JR P35	503047010	2008-07-09	132.97	−46.947	8.65 / –
VELA JR P36	503048010	2008-07-09	133.06	−47.224	9.36 / –
VELA JR P37	503049010	2008-07-09	132.61	−47.170	12.3 / –
VELA JR P38	503050010	2008-07-10	132.20	−47.231	10.4 / –
RXJ_0852−4622_NW	500010010	2005-12-19	132.29	−45.616	161 / 215
RXJ_0852−4622_NW_offset	500010020	2005-12-23	135.13	−47.910	54.5 / –

4.3 Data Reduction

4.3.1 XIS

In Vela Jr. obesrvatoin, spaced-row charge injections (Nakajima et al. (2008), Uchiyama et al. (2009), and section 3.2) were carried out in all the observations except NW and NW_offset. We use the software package `Heasoft 6.12` with `CALDB 2009-08-04` for the analysis and XSPEC v12.7.1 for the spectral analysis[1]. Each observation data is reprocessed by `aepipeline 1.0.1`. We extract events based on the following criteria: elevation angle from night earth $> 5°$, elevation angle from day earth $> 20°$. We remove calibration source regions at the corner of the FOV. After avobe reductions, we check light curve in order to find unusual event like incident of high energy particles from solar flare. There are not such events in all data.

4.3.2 HXD-PIN

We do not present the result of GSO because no significant detection is made. We use the same software package as XIS analysis. We extract events which have an elevation angle of $> 5°$, and geomagnetic cut-off rigidity of > 6 GV. Geometric cut-off rigidity is shield ability of earth magnetic field for incident cosmic ray from outer space. We check light curve as same as XIS analysis, and find no anomaly.

4.4 Estimation of Backgrounds

When we analyze the spectrum of source, we basically used the offset observation data or signal of outside of source region of source observation to subtract it from the on-source data. If any off-set observations are not available, for example due to source contaminations, we estimate the backgrounds described below and evaluate the effect. Here we cosider the cosmic X-ray background (CXB), the non X-ray background (NXB), and the galactic ridge X-ray emission (GRXE) as backgrounds.

The CXB is uniform X-ray emission from the whole sky. Giacconi et al. (1962) discovered

---

[1] https://heasarc.gsfc.nasa.gov/xanadu/xspec/

CXB with the Aerobee sounding rocket carrying three Geiger counters. At the present, thanks to many X-ray satellite such as ROSAT, Chandra, XMM-Newton, and ASCA, the 2–10 keV CXB has been almost resolved into discrete sources, leaving at most 10—-20% at the faintest flux limit (e.g. Mushotzky et al. (2000)). Some authors parameterized the spectral model of CXB. I use the models by Kushino et al. (2002) and Yoshino et al. (2009) in the XIS analysis, and Boldt & Leiter (1987a) in the HXD-PIN analysis.

The NXB is the instrumental background except for the celestial X-ray background. It consists of instrumental detector noise and particle background. High energy particles interact with the detectors and surrounding structure, and create background with a flat continuum and fluorescence lines. Therefore NXB has time variability depending on orbits (COR, passing SAA), the number of incident protons, and activations of heavy elements in the sensor (e.g. Gd and Bi). The NXB is a major part of backgrounds for HXD specifically. HXD team releases NXB model for each observation (Fukazawa et al. 2009). Users are able to verify a reproducibility of NXB model by comparing with count rate during earth occultation.

The GRXE is diffuse X-ray emission along with the Galactic plane (e.g. Cooke et al. (1969)). Its origin is still debated. The GRXE spectrum consists of at least two plasmas with different temperatures (Kaneda et al. 1997). Characteristics of both components do not change with increase of galactic longitude, while get dark with increase of galactic latitude. The GRXE spectrum at the Galactic center region has been discussed by some authors. I adopt the model by Yuasa et al. (2012) which shows analysis in both soft and hard X-ray band with Suzaku.

Chapter 5

Analysis and Results of Vela Jr.

Contents

5.1 XIS Analysis 45
5.1.1 Imaging Analysis 45
5.1.2 Spectral Analysis 46
5.2 HXD Analysis 47
5.2.1 Estimation of Reproducibility of NXB model 47
5.2.2 Calculation of Angular Response 50
5.2.3 Spectral Analysis 50
5.3 Joint Spectrum 55

5.1 XIS Analysis

5.1.1 Imaging Analysis

Figure 5.1 shows the mosaiced XIS image of Vela Jr. in 2–5 keV, which is created with `ximage`, combining the exposure and vignetting-effect corrected image of each observation. Shell structures of Vela Jr. are clearly visible. We focus on the NW shell, which is detected in TeV gamma-rays (Katagiri et al. 2005) and reportedly shows bright synchrotron X-ray

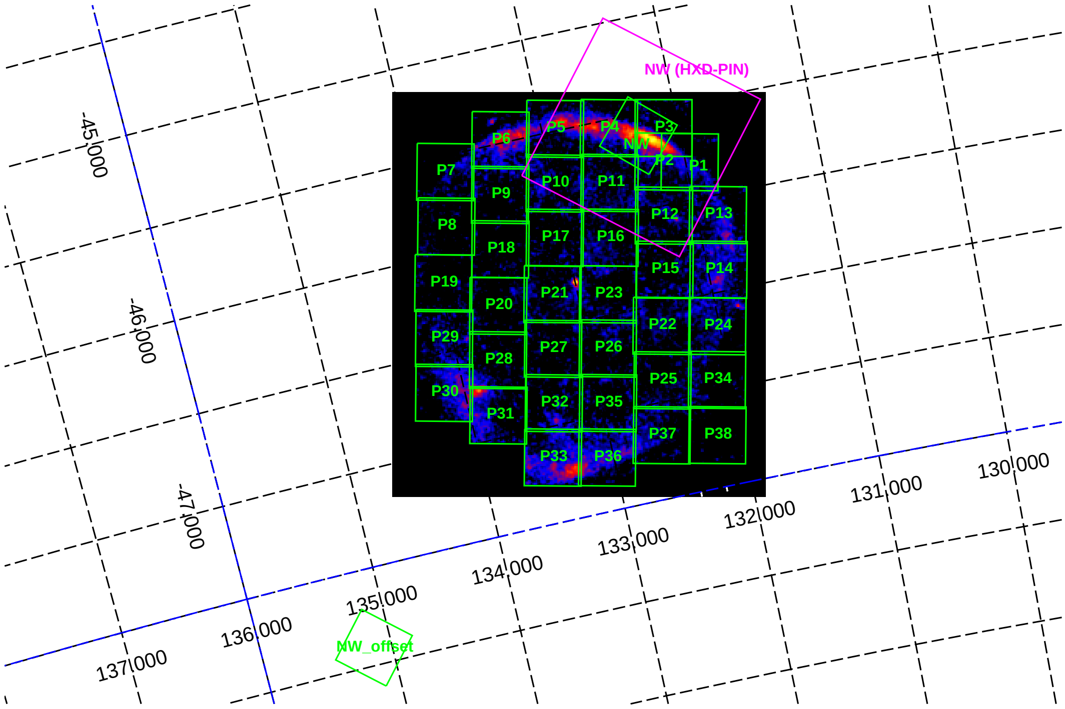
NW (HXD-PIN)
P1
P2
P3
P4
P5
P6
P7
P8
P9
P10
P11
P12
P13
P14
P15
P16
P17
P18
P19
P20
P21
P22
P23
P24
P25
P26
P27
P28
P29
P30
P31
P32
P33
P34
P35
P36
P37
P38
NW
NW_offset
-45.000
-46.000
-47.000
137.000
136.000
135.000
134.000
133.000
132.000
131.000
130.000

Figure 5.1: The mosaiced XIS image of Vela Jr. in 2–5 keV band. The exposure is corrected, but the CXB is not subtracted. The regions of the calibration sources are removed. The green and magenta boxes show the FOVs of the XIS of all the observations and of the PIN during NW observation, respectively. The coordinates are in the J2000 equatorial system.

filaments (Bamba et al. 2005a). In order to match the data with those of the HXD-PIN, we selected the region inside the FOV of the PIN NW observation, which is a square sky region with apexes of (133.37, −45.69), (132.17, −46.45), (131.09, −45.61) and (132.29, −44.86) in equatorial coordinates. Consequently, the entire regions of NW, P1, P2, P3, P4, P11 and P12, and parts of P5, P6, P9, P10, P13, P14, P15, P16 and P17 are included. The spectra are summed with `mathpha` in units of counts without exposure weighting. The errors are propagated as Poisson errors.

5.1.2 Spectral Analysis

We use the 2–8 keV band of XIS 0 and 3, and 2–7 keV of XIS 1, ignoring the energy band below 2 keV to avoid thermal contamination from Vela SNR (Hiraga et al. 2009). We consider the XIS backgrounds by comparing background spectra produced in the following four different methods: (i) NW_offset, (ii) CXB_Kushino + NXB_this, (iii) CXB_Yoshino + NXB_this, (iv) NW_offset − NXB_NW_offset + NXB_this, where NW_offset is the spectrum from the observation RX J0852−4622_NW_offset (table 4.2), CXB_Kushino and CXB_Yoshino denote the cosmic X-ray background estimated by Kushino et al. (2002) and Yoshino et al. (2009), respectively, and NXB denotes the non-X-ray background. The two NXBs of NXB_this and NXB_offset are estimated with `xisnxbgen`, which makes use of the NXB database of the night-earth observations by Tawa et al. (2008), extracting the data from 4 months before to 16 months after the observation, based on this and the NXB_offset observations, respectively.

Note that the model (i) is feasible, because all four background spectra are found to be consistently reproduced with a power-law model within 90% confidence level. The background (iv) is considered to take account of a potential time-variation of NXB. We ignore the energy range of 5.9 ± 0.2 keV in our analysis to eliminate scattered ^{55}Fe line from the decaying calibration source during the observations.

Response files are created with `marfrmf` from the redistribution matrix file (rmf) made by `xisrmfgen` and ancillary response file (arf) made by `xissimarfgen` (Ishisaki et al. 2007), based on the XIS 2–5 keV image file within the FOV of the PIN NW observation. We add all the XIS responses of each observation with the weight of each exposure.

We evaluate the background-subtracted XIS spectra by fitting with a power-law function with the Galactic absorption: `phabs*powerlaw`. The absorption column density is fixed to be 6.7×10^{21} cm^{-3}, which is the best-fit value derived by Hiraga et al. (2009), with the metal abundance adopted from Anders & Grevesse (1989). We then obtain acceptable results with χ^2/d.o.f. of 732.16/658 = 1.11. Figure 5.2 shows the XIS spectra, and Table 5.1 shows the best-fit parameters.

5.2 HXD Analysis

5.2.1 Estimation of Reproducibility of NXB model

To identify pointings which show significant hard X-ray signals with HXD-PIN, we compare the background-subtracted count-rates of each observation with the systematic error of the corresponding simulated background spectrum. We employ a modeled CXB by Boldt & Leiter (1987b) and simulated NXB spectrum with `hxdpinxbpi`, the latter of which is

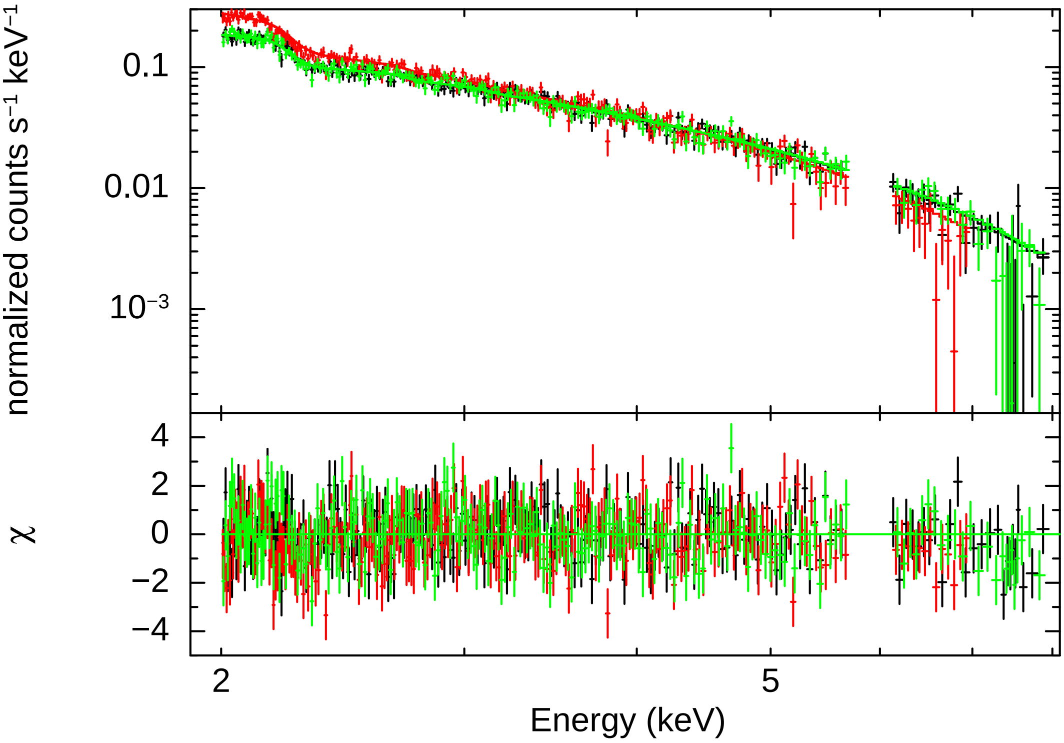

Figure 5.2: The upper panel shows the XIS spectra fitted with a single power-law model in the 2.0–8.0 keV band. The lower panel shows the χ-residuals between the data and best-fit model. The black, red, and green lines denote the XIS 0, 1, and 3 data, respectively.

Table 5.1: The best-fit parameters for a power-law model for the XIS spectra and the PIN spectrum.

Parameter	XIS$*^0$	HXD-PIN$\dagger^0$
Photon index	2.93 ± 0.02	$3.15^{+1.18}_{-1.14}$
flux [erg cm^{-2} s^{-1}]	$4.43 \pm 0.03 \times 10^{-11}\ddagger^0$	$8.26 \pm 1.44 \times 10^{-12}\S^0$
χ^2/d.o.f.	732.16/658	0.87/4

Notes. Errors are for a single parameter of interest in 90% confidence.

$*^0$The absorbing column density is set to be 6.7×10^{21}cm^{-2}, referring to Hiraga et al. (2009).
$\dagger^0$The model contains the fixed GRXE component and the normalization is corrected (see text).
$\ddagger^0$The flux at the range of 2–10 keV.
$\S^0$The flux at the range of 12–22 keV.

calculated on the basis of observed NXB spectrum during earth occultation. The expected uncertainty of the NXB model is reported as 3% in 10–60 keV by Fukazawa et al. (2009). The PIN detection significance is determined with the NXB reproducibility. Since hard X-ray sources RCW 38 and IGR J09026−4812 contaminate the NW_offset observation, those offset observations are not to used to estimate the NXB and CXB backgrounds for this HXD-PIN analysis. We ignore the energy band below 12 keV to avoid thermal noise. Consequently, we obtain 6 observations that exceed 1 σ significance level of NXB uncertainty in the 10–60 keV band: P1, P2, P3, P5, P13, and NW, all of which are located in the north-west of Vela Jr.

To confirm the detections, we re-evaluated uncertainty of the NXB model for each observation by comparing the count rate of CXB-subtracted signal with that of each simulated NXB in the 10–60 keV band. For the NXB, we derive the count rate during earth occultations during each observation. All but the NW contained some periods of earth occultations. For the NW observation, we used the earth occultation data obtained in the observations conducted immediately before and 26 hours after the NW observation: E0102–72 (ObsID 100044010) and NGC 4388 (ObsID 800017010). Comparing those with the count rate of the model, we estimate the systematic uncertainties of the NXB model to be ∼ 7%, 6%, 0.2%, 0.5%, 9%, and 1% for positions P1, P2, P3, P5, P13, and NW, respectively, in 10–60 keV. P1, P2, and P13 have larger uncertainty than the nominal value reported in Fukazawa et al. (2009) because the exposures of earth occultation were short. A significant emission to 21.9

keV from the position NW is detected at 3 σ confidence level, whereas those from the other observations are detected at only 0.5–1.5 σ level.

5.2.2 Calculation of Angular Response

In order to examine the PIN spectrum of diffuse objects, we need to calculate the effective areas for which the angular response is convolved ('arf' in the XSPEC), based on the source brightness distribution within the FOV. We assume that the spatial distribution in the hard X-ray band with PIN is the same as the CXB-subtracted XIS 2–5 keV images (section 5.1.2). The proper response of the PIN detectors has a pyramidal shape. However, for simplicity, we divide the spatial distribution within the PIN FOV by 9×9 grids and make 81 arfs in total with `hxdarfgen`, assuming that a point source centered in each section is responsible for the entire flux from the section in making an arf in each section. Then we sum up these arfs with `addarf` with weights calculated from the XIS image. Practically, this procedure is to approximate the original pyramidal angular response by 9×9 prisms. We calculate the ratio of the geometric integrations of the 81 prisms to the pyramid to be 0.8. Thus, the flux based on this arf should come out at the value $1/0.8 = 1.25$ times larger than the real one.

We validate this ratio of the normalizations with another pair of data sets: (A) the effective area derived with this method for the 9×9 section with a uniform weight, (B) that calculated from the numerically-simulated flat-sky response file, which is delivered by the HXD team. We confirm that the ratio of the former (A) to the latter (B) is $\sim$0.8 and so is consistent with the value calculated above.

Now that the method is validated, we make the arf for our HXD-PIN spectrum with this method, assuming the HXD-PIN spatial distribution of Vela Jr. to be the same as the CXB-subtracted brightness distribution observed with the XIS. We find that 39 out of the 81 sections inside Vela Jr. show no significant XIS signal and hence give them the weight of zero in calculating the arf for the HXD-PIN spectrum. Figure 5.3 displays the employed sections, and Table 5.2 lists the weights. All the flux and flux values presented hereafter are corrected for the above-mentioned factor.

5.2.3 Spectral Analysis

Using the arf for Vela Jr. NW with the officially delivered responses for the flat sky and a point source, we examine the observed hard X-ray spectrum in detail. First, we evaluate possible contamination of the galactic ridge X-ray emission (GRXE: Krivonos et al. (2007)), given the fact that Vela Jr. is on the Galactic plane. We use the NXB-subtracted XIS spectrum of the offset observation as the background template for the HXD data of Vela Jr. We fit it with, in addition to the fixed CXB model (Kushino et al. 2002), the GRXE model, for which we employ a photo-absorbed two temperature thermal plasma emission model. Assumed absorption column density $N_{\mathrm{H}} = 4.0 \times 10^{22}\mathrm{cm}^{-2}$ and the two temperature thermal plasma model (`apec` in XSPEC) with $kT = 1.66$ keV and 15.1 keV (Table 4 of Yuasa et al. (2012)). Considering the effective solid angle of PIN and XIS, we then estimate the GRXE component flux for the PIN spectrum (12 – 22 keV) and XIS spectrum (2 – 10 keV) to be 2.00×10^{-13} and 7.01×10^{-13} erg $\mathrm{cm}^{-2}\mathrm{s}^{-1}$, respectively. This estimated GRXE model is included in all the following model-fittings of the HXD-PIN spectrum. Note that the flux of GRXE in the XIS range is 0.3–0.6% of that from NW. Therefore, the effect of the GRXE to the XIS spectrum is negligible.

Second, we check the possible contamination from nearby hard X-ray sources. According to the INTEGRAL catalog[1], there was no contaminating point-source in the 18.3–59.9 keV range in the FOV of the HXD-PIN. The brightest diffuse source in the PIN FOV is Vela PWN below 10 keV (Katsuda et al. 2011). Mori et al. (2014) studied the spectrum of Vela PWN with the XIS observation of VELA PWN E7 (ObsID 506050010), and reported that the surface brightness is ~ 0.3 times CXB level and that the photon index is ~ 3.3. This flux corresponds to 5% of that of the NW in the 2–10 keV band, and hence our XIS spectrum is not significantly affected with the Vela PWN component within statistics. Extrapolating this spectrum to the energy band of the HXD-PIN, we find that the flux of Vela PWN is $\leq$ 2% of that of the NW in the 12–22 keV energy range, and therefore the contribution from the Vela PWN component is negligible for the PIN data. Therefore, we conclude that the detected signals are fully originated from Vela Jr. NW.

Finally we fit the background-subtracted HXD-PIN spectrum up to 22 keV with a single power-law model. Figure 5.4 shows the spectrum with the best-fit model. The systematic error of the NXB model of 1%, which is derived based on the earth occultation data, is included in errors of the source spectrum. The spectrum is well reproduced by a single power-law model with χ^2/d.o.f. ~ 0.22. The best-fit photon index is $3.16^{+1.09}_{-1.15}$and the flux is $(8.15 \pm 1.40) \times 10^{-12}$ erg cm^{-2} s^{-1} in 12–22 keV, as listed in table 5.1. Here the errors due to the model-fitting error of the GRXE are 0.006% for the photon index and 0.02% for normalization.

---

[1] http://www.isdc.unige.ch/integral/science/catalogue

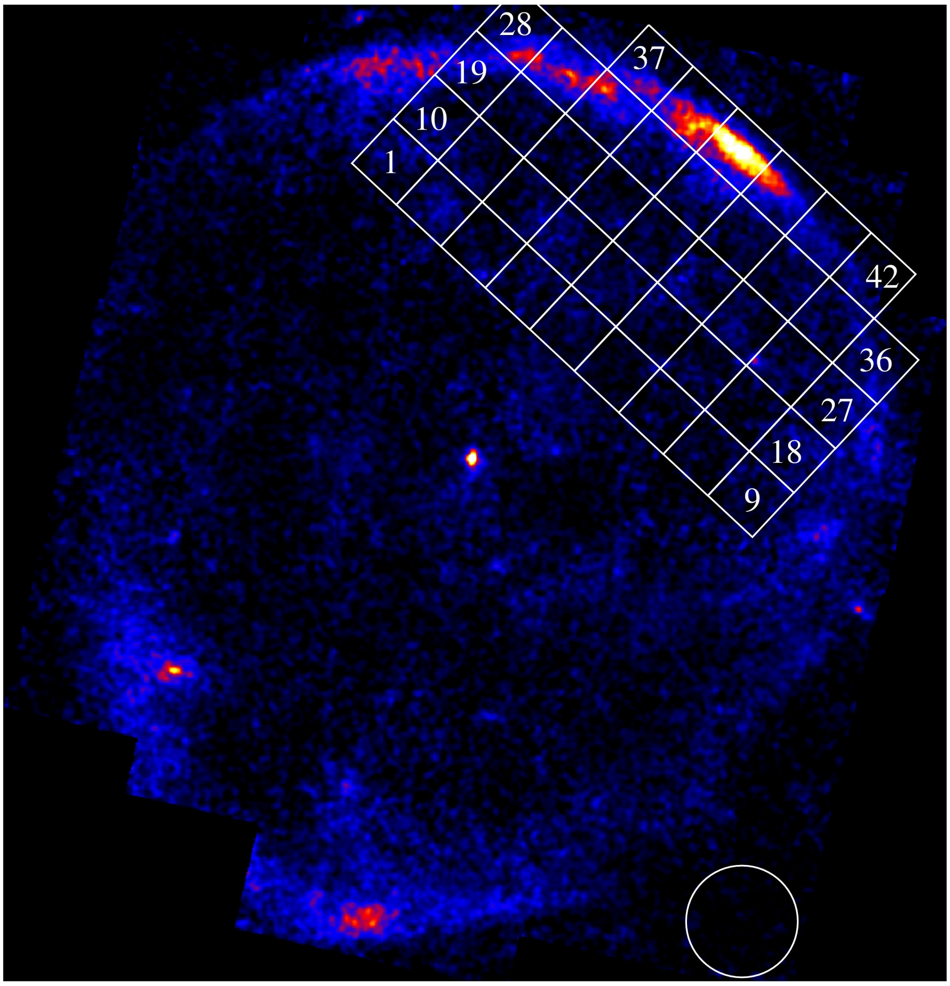

Figure 5.3: Forty-two white boxes used to estimate the arf, in which the significant X-ray emission was detected with the XIS (see text). A white circle is the region for estimating the background. The image is the same as Figure 5.1.

Table 5.2: The weights for making arfs of the PIN. The pointing IDs are shown in figure 5.3.

Pointing ID	weight	Pointing ID	weight
1	0.018	22	0.012
2	0.020	23	0.013
3	0.012	24	0.017
4	0.014	25	0.016
5	0.013	26	0.016
6	0.009	27	0.021
7	0.009	28	0.033
8	0.009	29	0.068
9	0.015	30	0.053
10	0.019	31	0.028
11	0.013	32	0.032
12	0.014	33	0.016
13	0.017	34	0.016
14	0.015	35	0.018
15	0.013	36	0.021
16	0.013	37	0.034
17	0.009	38	0.076
18	0.022	39	0.119
19	0.034	40	0.051
20	0.013	41	0.022
21	0.010	42	0.008

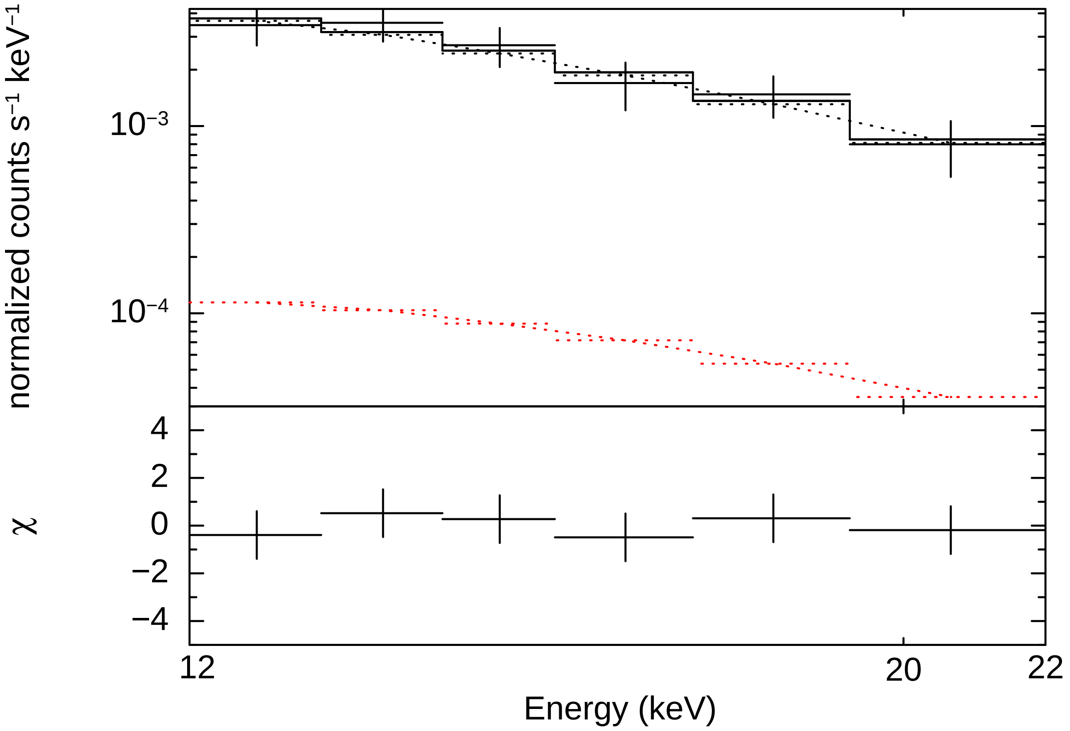

Figure 5.4: The black points in the upper panel show the HXD-PIN spectrum fitted with single power-law model in 12.0–22.0 keV band. The error bars include also the systematic error of the NXB model. The red dotted line shows the contribution from the modeled GRXE. The lower panel shows the χ residuals between the data and best-fit model.

5.3 Joint Spectrum

In sections 5.1 and 5.2, we have derived the spectral parameters independently with the XIS and PIN. We then fit the XIS and PIN spectra simultaneously to give further constraints, making use of the best available statistics.

First, we apply a single power-law model, referred to as model (i) in Table 5.3, linking the photon index for the XIS and PIN spectra. Ishida et al. (2007)[2] reported that the normalization factors differed between the XIS and PIN spectra for the point-like source Crab, which has a power-law spectrum, and that their ratio of the PIN to the XIS (henceforth referred to as the cross-normalization) was 1.13. Thus, we link the power-law normalizations of the XIS and PIN spectra with the ratio of 1/1.13 in the model-fitting. Figure 5.5 shows the spectra and the best-fit model, and Table 5.3 lists the best-fit parameters.

The X-ray spectra of several SNRs have rolloff structures (e.g. Takahashi et al. (2008), Tanaka et al. (2008), Bamba et al. (2008), Zoglauer et al. (2015a)). Although the above result on a single power-law model does not require any spectral bending in the 2–22 keV band, we further try to examine a possible spectral curvature with various models listed in Table 5.3, setting the cross-normalization to 1.13 (see the previous sub-section). Table 5.3 shows the best-fit parameters of each model. Four panels in figure 5.5 show the spectrum overlaid with the best-fit model spectra for 4 different models. The parameters with the cutoff power-law (`cutoffpl` in XSPEC) which is a power-law model with high energy exponential rolloff (ii) are consistent with the results with the single power-law model (i), because the best-fit roll-off energy of 146 keV is out of the range. Fitting with the broken power-law model (iii; `bknpower` in XSPEC) implies the breaking energy of 7.90 ± 0.18 keV with a change of spectral index of -0.3, although it is still consistent with the results of individual fittings with the XIS and PIN, and with the wide-band fittings with the models (i) and (ii), within errors.

---

[2] http://www.astro.isas.ac.jp/suzaku/doc/suzakumemo/suzakumemo-2007-11.pdf

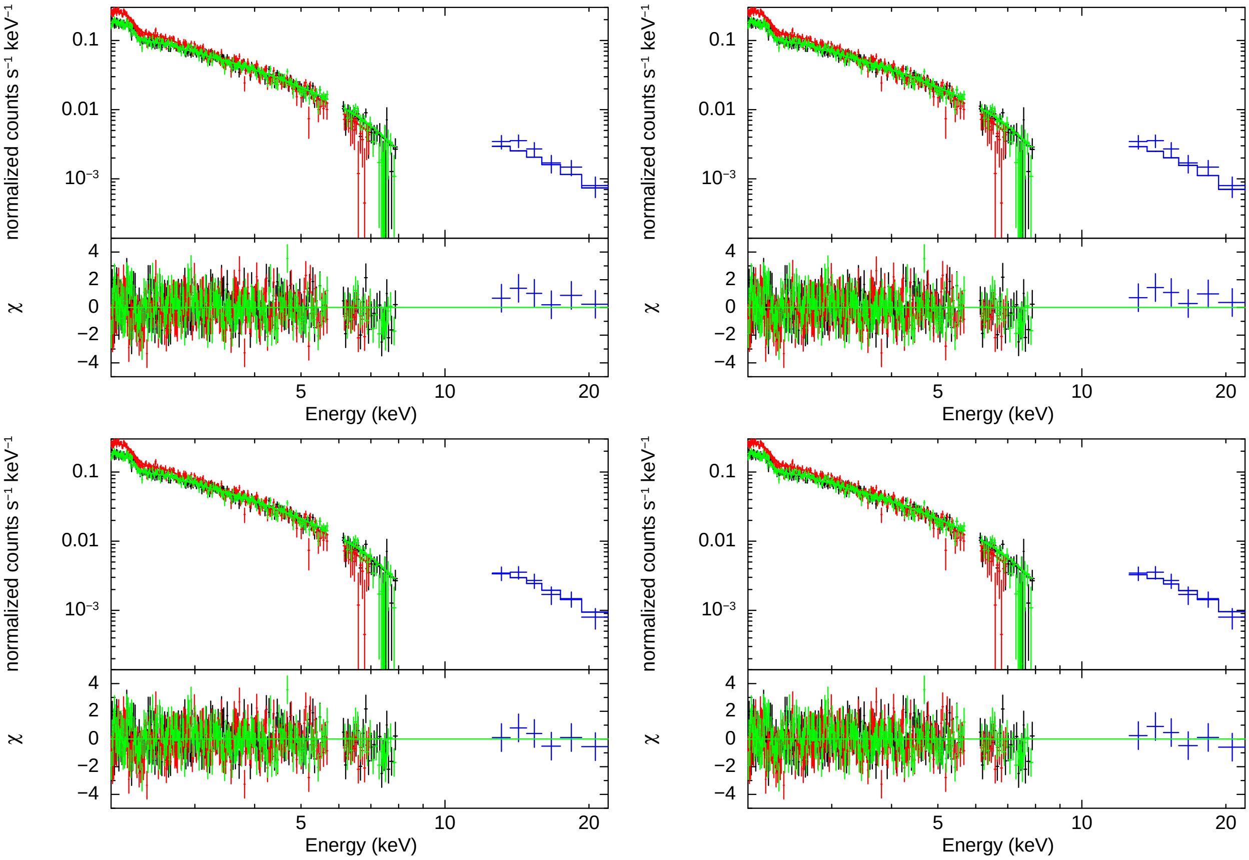

Figure 5.5: Upper left: The upper panel shows the wide band spectrum fitted with (i) single power-law model in 12.0–22.0 keV band. The systematic error of NXB model is included. The cross normalization is fixed at 1.13, which is the value for a point source. The lower panel shows the residuals between the data and model. Upper right: Same as the upper left except for using (ii) cutoff power-law model. Lower left: Same as the upper left except for using (iii) broken power-law. Lower right: Same as the upper left except for using (iv) 10 keV broken power-law.

Table 5.3: The best-fit parameters for the XIS and PIN spectra.

Parameters	(i) SPL	(ii) CPL	(iii) BPL	(iv) 10BPL
Photon index$_{\mathrm{allorsoft}}$	2.92 ± 0.01	2.90 ± 0.01	2.93 ± 0.01	2.93 ± 0.01
Photon index$_{\mathrm{hard}}$	–	–	2.66 ± 0.03	$2.56^{+0.42}_{-0.34}$
rolloff energy [keV]	–	> 131	–	–
breaking energy [keV]	–	–	7.90 ± 0.18	10.0 (fixed)
flux$_{\mathrm{10keV}}$ [$\times 10^{-5}$ Jy]	5.05 ± 0.03	4.92 ± 0.03	5.30 ± 0.03	4.99 ± 0.03
χ^2/ d.o.f.	736.51/664	735.69/663	733.59/662	733.85/663

Notes. The model names are abbreviated as following; single power-law is SPL, cutoff power-law is CPL, broken power-law is BPL, and 10 keV broken power-law is 10BPL. The absorbing column density is set to be $6.7 \times 10^{21}\mathrm{cm}^{-2}$, referring to Hiraga et al. (2009). Cross-normalization factor of HXD-PIN is fixed at 1.13, which is the value for a point source. Errors are for a single parameter of interest in 90 % confidence.

Chapter 6

Discussion

Contents

6.1 Vela Jr. 59

6.2 Relation of photon indices described by Yamazaki et al. 60

6.3 Imaging analysis of the outlier SNRs 62

6.1 Vela Jr.

In section 5, we have shown the results of spectral analysis of Vela Jr. with Suzaku. X-rays with the energy up to 22 keV are detected from the north-west region of Vela Jr. The spectra in the soft and hard X-ray band are reproduced with a power-law model with the photon indices of 2.93 ± 0.02 and $3.15^{+1.18}_{-1.14}$, respectively. When the spectra in both the bands are fitted simultaneously, a single power-law model with the photon index of 2.92 ± 0.01, or a slightly concave-shaped broken power-law model, is accepted.

The obtained wide band steep power-law like spectrum with photon index ~ 3 implies the energy index $p \sim 5$ of synchrotron electron with the energy distribution of $\mathrm{d}N/\mathrm{d}E \propto E^{-p}$. This steep spectrum strongly suggests that the rolloff energy is well below the XIS band. Combi et al. (1999) reported the radio spectral index of $\alpha = 0.3 \pm 0.3$ at NW region, and Duncan & Green (2000) reported the flux density at 1 GHz of ~ 50 Jy from entire region of the SNR. In order to verify consistency between the X-ray and radio results, the X-ray spectra with XIS and PIN are tested with `srcut` model in XSPEC (Reynolds 1998b). The `srcut` model describes the synchrotron spectrum from electrons with an exponentially-rolloff power-law distribution in energy. The synchrotron spectrum has a power-law form from radio band to X-ray band with a rolloff energy. The `srcut` model has three parameters; X-ray rolloff energy, spectral index at 1 GHz, and flux at 1 GHz. We fit the X-ray spectra using spectral index α in radio band reported by Combi et al. (1999) and typical value of young SNRs, i.e., $\alpha = 0.3$ and $\alpha = 0.6$, respectively. Then, when $\alpha = 0.3$, the best fit parameters of 1 GHz flux density and rolloff energy of 0.15 ± 0.01 Jy and 0.15 ± 0.01 keV with χ^2/d.o.f. of 1.18. When $\alpha = 0.6$, these are $31.6^{+1.8}_{-1.9}$ Jy and 0.27 ± 0.01 keV with χ^2/d.o.f. of 1.17. The area of NW region in this paper is ~ 27 % of entire Vela Jr., hence the 1 GHz flux is expected to become smaller than values reported by Duncan & Green (2000) which is derived from emission of entire Vela Jr. Actually the derived radio flux is smaller than the value of entire Vela Jr. reported by Duncan & Green (2000). In addition, rolloff energy is below the XIS band, which is consistent with our X-ray analysis. Therefore results of our X-ray analysis and in radio band are consistent each other. Since the radio flux at NW region alone has not been reported, additional radio observation is needed to verify this result on wideband spectrum of the NW region.

Lastly, we show flux comparison with TeV emission. In section 5, we derived the flux of $(4.43 \pm 0.03) \times 10^{-11}$erg cm^{-2} s^{-1} in 2–10 keV band while Aharonian et al. (2007) showed the TeV flux of entire Vela Jr. of $(15.2 \pm 0.7 \pm 3.20) \pm 10^{-12}$cm^{-2}s^{-1} with H.E.S.S. Both band spectra exhibit similar slope and the X-ray to TeV gamma-ray flux ratio is ~ 2.91. If we assume the cosmic microwave background inverse Compton scattering as TeV emission mechanism, we estimate the magnetic field $B \sim 5.5\ \mu$G, which is consistent value derived by Kishishita et al. (2013) and Lee et al. (2013). If the TeV emission is hadronic, the field strength is not constrained and it may be much higher (Bamba et al. 2005a).

6.2 Relation of photon indices described by Yamazaki et al.

As we saw in chapter 2, steep X-ray spectrum commonly observed in X-ray band naturally requires concave rolloff shape, as far as we assume simple acceleration/synchrotron cooling mechanism. Yamazaki et al. (2014) proposed a simple diagnostic to find possible acceleration mechanisms from the observed spectral shape near the maximum energy, assuming (a) one-zone, (b) electron energy spectrum of an exponential cutoff power-law ($N(E) \propto E^{-p} \exp[-(E/E_{\rm max,e})^a]$) expressed as equation 1 in Yamazaki et al. (2014), and (c) synchrotron radiation. Figure 5 in Yamazaki et al. (2014) shows the relation between the electron spectral parameters p and a on the relation of soft and hard X-ray spectral indices. They calculated the soft and hard spectrum indices expected with the electron energy index $2.3 < p < 3.3$ and $0.5 < a < 4$.

In order to discuss theoretical models, we evaluated the Vela Jr. X-ray spectra by fitting with a broken power-law model (iv) with the fixed breaking energy to 10 keV. Table 5.3 shows the best-fit parameters of this model, and lower right panel of Figure 5.5 is the spectrum overlaid with the best-fit model spectra. Both the derived photon indices are consistent with that obtained with the model (iii), though that in the hard band is marginally smaller by 0.1 than the latter. The best-fit flux is close to that obtained in the models (i) and (ii).

Figure 6.1 overlays our results of the photon indices of below and above 10 keV in the model (iv) in red on Figure 5 in Yamazaki et al. (2014). In addition to our result from Vela Jr., we added plots for the young, free expansion phase, TeV emitting, shell type SNRs, G1.9+0.3 (Zoglauer et al. 2015b), Tycho SNR (Tamagawa et al. 2009b) and SN 1006 (Allen et al. 2001). The soft and hard photon indices are estimated from the reported best fit spectrum parameters.

- SNRs RX J1713.7−3946 and Cassiopeia A are originally indicated in Yamazaki et al. (2014).
- SNRs RX J1713.7−3946, G1.9+0.3 or Tycho SNR are reported that their spectral shapes are well described with a synchrotron radiation cut off model (srcut). The best fit paramters of the srcut model are directory converted to one of the the theoretical lines in the diagram.
- SNR Vela Jr. are indicated according to the models (iv) (red cross).

Similar to Cassiopeia A originally indicated in Yamazaki et al. (2014), we see two SNRs (Cas A, Vela Jr. and SN 1006) which do not fit any of the theoretical-model lines by Yamazaki et al. (2014), despite the X-ray spectrum is above "rolloff" energy estimated by comparison of spectral indices in radio and X-ray bands. These right lower region outlier of the diagram implies $p > 3.3$ and/or smaller $a < 0.5$, as far as we assume the scheme described in Yamazaki et al. (2014). The larger p, however, requires higher compression rate and smaller a requires much lower energy dependence of diffusion coefficient than that expected in the Bohm condition. Both of these requirements apparently contradict the simple one zone acceleration/cooling model by Yamazaki et al. (2014). Therefore a possible cause for the mismatch is that at least one of the assumptions (a), (b) and (c) is inadequate for these 'outliers'. A normal one-zone synchrotron X-ray spectrum usually has a photon index of ~ 2 in a softer energy band and rolls off toward the harder energy band due to cooling or escape. However the wide-band X-ray spectrum of each 'outlier' SNR is well reproduced with a single power-law or even a concave-shape broken power-law. It may suggest that combination of more than one emission component and/or complex emission mechanisms creates the observed X-ray spectra (Longair (1994), Drury et al. (1999), Zirakashvili & Aharonian (2007), Malkov & Drury (2001b), Toptygin & Fleishman (1987), Medvedev (2000), Reville & Kirk (2010), Teraki & Takahara (2011), Yamazaki et al. (2006), Laming (2001), Vink & Laming (2003), Vink (2008), Ohira et al. (2012)).

Before closing this section, we validated the cross-normalization between the XIS and the PIN, since the analysis process of Vela Jr. was rather complex. We fit the spectra, allowing both the XIS and PIN normalizations to vary independently, and find that the best-fit photon index and the XIS flux are consistent with the above-discussed case within the error range, whereas the derived cross-normalization factor is 1.4 ± 0.3, which is marginally larger than that reported for the point source. This result may imply that brightness distribution in hard X-rays is more compact than that of the XIS image and that we have actually underestimated the PIN effective area, as we have assumed a larger diffuse-emission region than the real one. Considering the case of more compact hard X-ray brightness distribution than that of soft X-rays, we also showed a conservative fitting result with freed cross-normalization factor in figure 6.1 with blue mark and error bars. The best-fit photon indices are 2.93 ± 0.04 and $3.16^{+2.44}_{-2.20}$ in the soft and hard energy range, respectively. Although this estimation accepts most of the model lines presented in Yamazaki et al. (2014), it requires more than one emission region or complex emission mechanisms, again.

6.3 Imaging analysis of the outlier SNRs

By investigating the wide band X-ray spectrum curvature, we sorted out Vela Jr. and two SNRs indicating steep power-law like X-ray spectrum without signs of rolloff on the previous subsection. It suggests that emission regions of these outlier SNRs accept no simple one zone

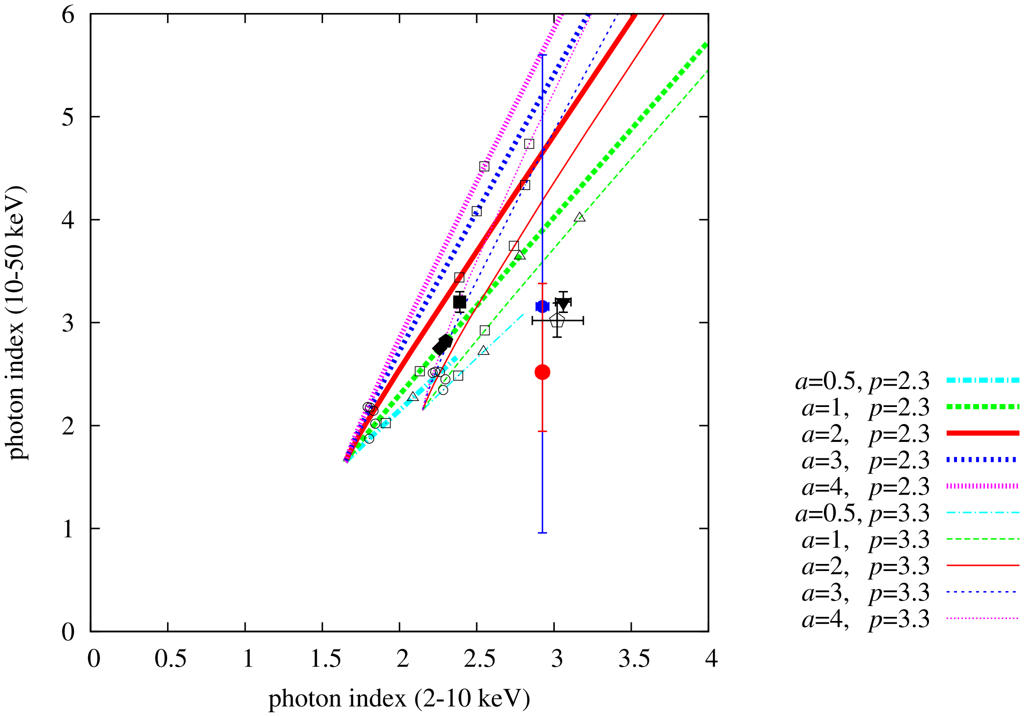

Figure 6.1: The relation between the two X-ray photon indices for soft and hard bands for a breaking power-law model. The straight lines show the theoretical lines derived by Yamazaki et al. (2014). The open squares, triangles and circles are for $BE^2_{\rm max,e} = 10^4$, 10^5, and $10^6 \mu{\rm G(TeV)}^2$, respectively (See Yamazaki et al. (2014)). The black squares and triangles show the result of RX J1713.7−3946 and of Cassiopeia A, respectively. The red and blue circles show this result with model (iv) with cross-normalization fixed to 1.13 or freed, respectively. These error bars show 99% confidence level.

synchrotron emission but multi-zone and/or multi emission mechanism, unlike other SNRs exhibiting expected rolloff shape. The X-ray emission region in the shell is recognized as sum of filaments by high resolution X-ray imaging. In order to investigate possible spatial inhomogeneity of the emission region, here we summarize the reported scale length of filament in the shell of each SNRs. We refered the filament widths reported by following: Bamba et al. (2005a) for Vela Jr., Bamba et al. (2005b) for Cas A and Tycho, Bamba et al. (2003) for SN1006, and Helder et al. (2012) for G1.9+0.3 and RX J1713.7−3946. Figure 6.2 shows the up-stream/down-stream filament widths of each SNR to be along with diameter of the shell. Most of the scale length of filament are almost in proportional to the diameter except up-stream length of the three outlier indicating slow evolution along with the diameter. Bamba (2004) discovered the scale length of the non-thermal filaments evolves wider as SNRs get older, at a rate of $t_{age}^{0.5}$ in upstream and faster in down stream. She pointed out that the scale length of filaments is expeted to be in proportional to the age in free-expansion-phase but the rate is to be reduced in for example Sedov phase ($t_{age}^{0.4}$). Since our sample is limited to the free-expansion-phase SNRs, the faster evolution of scale length is natural. However the slower evolution of filament scale length may implies local deceleration of the shock front by circum-stellar matter, and which may cause suggested inhomogeneity in physical state of emission regions.

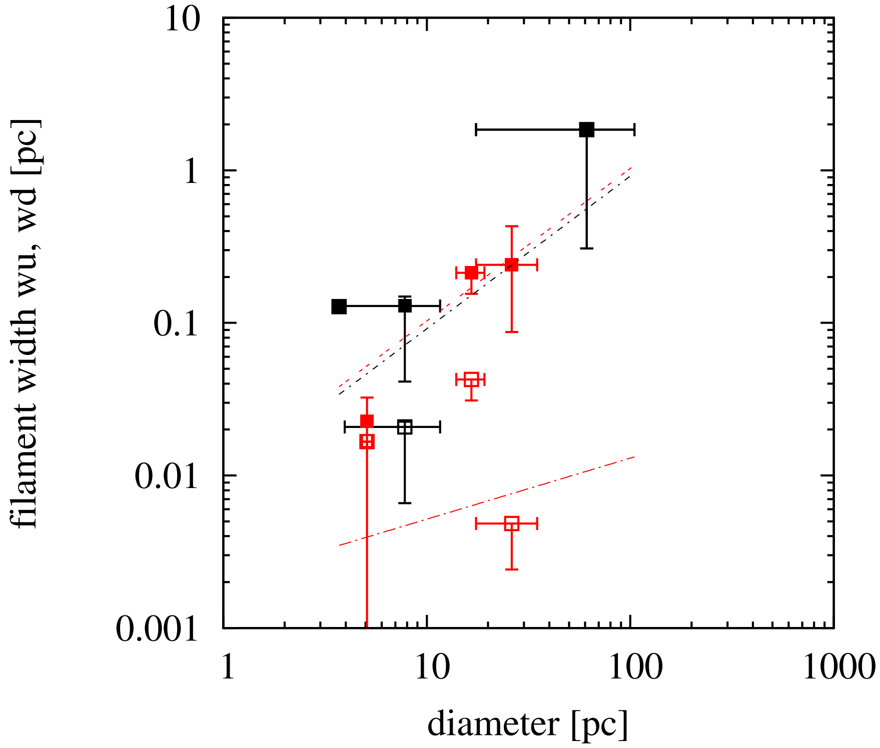

Figure 6.2: The relation between the diameter and filament width. The red shows outlier and the black shows other SNRs. The filled marker shows w_d and another shows w_u.

Chapter 7

Conclusion

- In this paper we summerized the hard X-ray observations of 6 SNRs which have effective particle acceleration during free expansion phase.
- In particular we succeeded in detecting hard X-ray spectrum up to 20 keV from Vela Jr. with Suzaku HXD.
  1. The photon indices of power-law components in soft and hard X-ray bands are independently derived as 2.93 ± 0.02 at 2–8 keV, and $3.15^{+1.18}_{-1.14}$ at 12–22 keV, respectively.
  2. Also the wide band X-ray spectrum ranging 2 – 22 keV band is well reproduced by a single power-law model or a concave broken power-law model.
- Three of six wideband spectra are expressed by simple synchrotron one-zone model.
- Other 3 samples are indicated that any of 3 premises, one-zone, electron distribution by shock acceleration, and synchrotron emission, is not satisfied.
- The all of filament width of these 3 samples are nallow in upstream of shock and show the deviation from free expansion. This is not contradict of the characteristics which require some non-homogeneity.

Bibliography

Abdo, A. A., Ackermann, M., Ajello, M., et al. 2010, , 710, L92

Aharonian, F., Akhperjanian, A. G., Bazer-Bachi, A. R., et al. 2005, *Astronomy & Astrophysics*, 437, L7

Aharonian, F., Akhperjanian, A. G., Bazer-Bachi, A. R., et al. 2007, *Astrophysical Journal*, 661, 236

Aharonian, F. A., Akhperjanian, A. G., Barrio, J. A., et al. 2001, *Astronomy & Astrophysics*, 373, 292

Allen, G. E., Petre, R., & Gotthelf, E. V. 2001, *Astrophysical Journal*, 558, 739

Anders, E. & Grevesse, N. 1989, , 53, 197

Aschenbach, B. 1998, , 396, 141

Axford, W. I. 1981, International Cosmic Ray Conference, 12, 155

Bamba, A., Fukazawa, Y., Hiraga, J. S., et al. 2008, *Publication of Astronomical Society of Japan*, 60, S153

Bamba, A., Yamazaki, R., & Hiraga, J. S. 2005a, *Astrophysical Journal*

Bamba, A., Yamazaki, R., Ueno, M., & Koyama, K. 2003, *Astrophysical Journal*, 589, 827

Bamba, A., Yamazaki, R., Yoshida, T., Terasawa, T., & Koyama, K. 2005b, *Astrophysical Journal*, 621, 793

Bandiera, R. & Petruk, O. 2004, *Astronomy & Astrophysics*, 419, 419

Bell, A. R. 1978, *Monthly Notices of the Royal Astronomical Society*, 182, 147

Blandford, R. & Eichler, D. 1987, , 154, 1

Boldt, E. & Leiter, D. 1987a, , 322, L1

Boldt, E. & Leiter, D. 1987b, , 322, L1

Chevalier, R. A. 1982a, *Astrophysical Journal*, 258, 790

Chevalier, R. A. 1982b, *Astrophysical Journal*, 259, 302

Combi, J. A., Romero, G. E., & Benaglia, P. 1999, , 519, L177

Cooke, B. A., Griffiths, R. E., & Pounds, K. A. 1969, , 224, 134

Drury, L. O. 1983, Reports on Progress in Physics, 46, 973

Drury, L. O., Duffy, P., Eichler, D., & Mastichiadis, A. 1999, *Astronomy & Astrophysics*, 347, 370

Duncan, A. R. & Green, D. A. 2000, *Astronomy & Astrophysics*, 364, 732

Ferrand, G. & Safi-Harb, S. 2012, Advances in Space Research, 49, 1313

Fink, H. H., Asaoka, I., Brinkmann, W., Kawai, N., & Koyama, K. 1994, *Astronomy & Astrophysics*, 283, 635

Friedman, H., Byram, E. T., & Chubb, T. A. 1967, Science, 156, 374

Fukazawa, Y., Mizuno, T., Watanabe, S., et al. 2009, *Publication of Astronomical Society of Japan*, 61, S17

Fukui, Y. 2013, in Astrophysics and Space Science Proceedings, Vol. 34, Cosmic Rays in Star-Forming Environments, ed. D. F. Torres & O. Reimer, 249

Giacconi, R., Gursky, H., Paolini, F. R., & Rossi, B. B. 1962, Physical Review Letters, 9, 439

Hanbury Brown, R. & Hazard, C. 1952, , 170, 364

Helder, E. A., Vink, J., Bykov, A. M., et al. 2012, , 173, 369

Hiraga, J. S., Kobayashi, Y., Tamagawa, T., et al. 2009, *Publication of Astronomical Society of Japan*, 61, 275

Ishisaki, Y., Maeda, Y., Fujimoto, R., et al. 2007, *Publication of Astronomical Society of Japan*, 59, 113

Kaneda, H., Makishima, K., Yamauchi, S., et al. 1997, *Astrophysical Journal*, 491, 638

Katagiri, H., Enomoto, R., Ksenofontov, L. T., et al. 2005, , 619, L163

Katsuda, S., Mori, K., Petre, R., et al. 2011, *Publication of Astronomical Society of Japan*, 63, S827

Kishishita, T., Hiraga, J., & Uchiyama, Y. 2013, *Astronomy & Astrophysics*, 551, A132

Koyama, K., Petre, R., Gotthelf, E. V., et al. 1995, , 378, 255

Koyama, K., Tsunemi, H., Dotani, T., et al. 2007, *Publication of Astronomical Society of Japan*, 59, 23

Krivonos, R., Revnivtsev, M., Churazov, E., et al. 2007, *Astronomy & Astrophysics*, 463, 957

Kushino, A., Ishisaki, Y., Morita, U., et al. 2002, *Publication of Astronomical Society of Japan*, 54, 327

Laming, J. M. 2001, *Astrophysical Journal*, 546, 1149

Lee, S.-H., Slane, P. O., Ellison, D. C., Nagataki, S., & Patnaude, D. J. 2013, *Astrophysical Journal*, 767, 20

Longair, M. S. 1981, High energy astrophysics

Longair, M. S. 1994, High energy astrophysics. Vol.2: Stars, the galaxy and the interstellar medium

Lopez, L. A., Grefenstette, B. W., Reynolds, S. P., et al. 2015, *Astrophysical Journal*, 814, 132

Malkov, M. A. & Drury, L. O. 2001a, Reports on Progress in Physics, 64, 429

Malkov, M. A. & Drury, L. O. 2001b, Reports on Progress in Physics, 64, 429

Medvedev, M. V. 2000, *Astrophysical Journal*, 540, 704

Minkowski, R. 1957, in IAU Symposium, Vol. 4, Radio astronomy, ed. H. C. van de Hulst, 107

Minkowski, R. 1966, *Astronomical Journal*, 71, 371

Mitsuda, K., Bautz, M., Inoue, H., et al. 2007, *Publication of Astronomical Society of Japan*, 59, 1

Mori, K., Katsuda, S., Uchida, H., & Tsunemi, H. 2014, in Suzaku-MAXI 2014: Expanding the Frontiers of the X-ray Universe, ed. M. Ishida, R. Petre, & K. Mitsuda, 52

Mushotzky, R. F., Cowie, L. L., Barger, A. J., & Arnaud, K. A. 2000, , 404, 459

Nakajima, H., Yamaguchi, H., Matsumoto, H., et al. 2008, *Publication of Astronomical Society of Japan*, 60, S1

Ohira, Y., Kohri, K., & Kawanaka, N. 2012, *Monthly Notices of the Royal Astronomical Society*, 421, L102

Petruk, O. 2005, Journal of Physical Studies, 9, 364

Petruk, O., Orlando, S., Beshley, V., & Bocchino, F. 2011, *Monthly Notices of the Royal Astronomical Society*, 413, 1657

Reville, B. & Kirk, J. G. 2010, *Astrophysical Journal*, 724, 1283

Reynolds, S. P. 1998a, in 19th Texas Symposium on Relativistic Astrophysics and Cosmology, ed. J. Paul, T. Montmerle, & E. Aubourg

Reynolds, S. P. 1998b, *Astrophysical Journal*, 493, 375

Shklovskii, I. S. 1953, Radioastronomiia.

Slane, P., Hughes, J. P., Edgar, R. J., et al. 2001, *Astrophysical Journal*, 548, 814

Takahashi, T., Abe, K., Endo, M., et al. 2007, *Publication of Astronomical Society of Japan*, 59, 35

Takahashi, T., Tanaka, T., Uchiyama, Y., et al. 2008, *Publication of Astronomical Society of Japan*, 60, S131

Tamagawa, T., Hayato, A., Nakamura, S., et al. 2009a, *Publication of Astronomical Society of Japan*, 61, S167

Tamagawa, T., Hayato, A., Nakamura, S., et al. 2009b, *Publication of Astronomical Society of Japan*, 61, S167

Tanaka, T., Uchiyama, Y., Aharonian, F. A., et al. 2008, *Astrophysical Journal*, 685, 988

Tawa, N., Hayashida, K., Nagai, M., et al. 2008, *Publication of Astronomical Society of Japan*, 60, S11

Teraki, Y. & Takahara, F. 2011, , 735, L44

Toptygin, I. N. & Fleishman, G. D. 1987, , 132, 213

Truelove, J. K. & McKee, C. F. 1999, *Astrophysical Journal Supplement*, 120, 299

Uchiyama, H., Ozawa, M., Matsumoto, H., et al. 2009, *Publication of Astronomical Society of Japan*, 61, S9

Uchiyama, Y., Aharonian, F. A., Tanaka, T., Takahashi, T., & Maeda, Y. 2007, , 449, 576

Vink, J. 2008, *Astronomy & Astrophysics*, 486, 837

Vink, J. & Laming, J. M. 2003, *Astrophysical Journal*, 584, 758

Völk, H. J., Berezhko, E. G., Ksenofontov, L. T., & Rowell, G. P. 2002, *Astronomy & Astrophysics*, 396, 649

Yamazaki, R., Kohri, K., Bamba, A., et al. 2006, *Monthly Notices of the Royal Astronomical Society*, 371, 1975

Yamazaki, R., Ohira, Y., Sawada, M., & Bamba, A. 2014, Research in Astronomy and Astrophysics, 14, 165

Yoshino, T., Mitsuda, K., Yamasaki, N. Y., et al. 2009, *Publication of Astronomical Society of Japan*, 61, 805

Yuasa, T., Makishima, K., & Nakazawa, K. 2012, *Astrophysical Journal*, 753, 129

Zirakashvili, V. N. & Aharonian, F. 2007, *Astronomy & Astrophysics*, 465, 695

Zoglauer, A., Reynolds, S. P., An, H., et al. 2015a, *Astrophysical Journal*, 798, 98

Zoglauer, A., Reynolds, S. P., An, H., et al. 2015b, *Astrophysical Journal*, 798, 98

Acknowledgements

First of all, I would like to thank supervisor professor Makoto S. Tashiro. I also have had the support and guidance of associate professor Yukikatsu Terada. They always gave me precious opinions and guided me kindly and politely.

I would like to thank associate professor Aya Bamba, Dr. Satoru Katsuda, associate professor Ryo Yamazaki, Dr. Yutaka Ohira, and Dr. Wataru Iwakiri for analysis of Vela Jr. They gave me technical opinion and some useful documents.

Finally, I would like to show my greatest appreciation to my family for supporting and understanding me.